Supporting Information

Angular Strain-Induced Polarization in a Ferroelectric Ammonium Cyclic-Phosphate and its Wind Speed Sensing Application

Vikash Kushwaha, [a] Darshan Yuvraj Sawant, [a] Antony Sylvester Kirana,[a] Subham Kumar Mahato,[a] Jan K. Zaręba,[b]* and Ramamoorthy Boomishankar [a] *

[a]Department of Chemistry, Indian Institute of Science Education and Research, Pune
Dr. Homi Bhabha Road, Pune – 411008, India.
E-mail: boomi@iiserpune.ac.in

[b]Institute of Advanced Materials Faculty of Chemistry, Wroclaw University of Science and Technology Wroclaw 50- 370, Poland.

Email: jan.zareba@pwr.edu.pl

Table of Contents

Experimental Section:

General Remarks

The starting materials (4S)-4-(2-Chlorophenyl)-2-hydroxy-5,5-dimethyl-1,3,2-diaxaphosphinate 2-oxide, 2-hydroxy-5,5-dimethyl-1,3,2-diaxaphosphinate 2-oxide, and benzylamine were purchased from the BLD Pharma and TCI chemicals, and used as received. The polymer polycaprolactone (PCL) was purchased from Sigma Aldrich and used as received. NMR spectra were recorded on a Bruker 400 MHz spectrometer (^{1}H NMR: 400.13 MHz, ^{13}C{^{1}H} NMR: 100.62 MHz,^{31}P{^{1}H} NMR: 161.97 MHz) at room temperature using $SiMe_4$ (^{1}H, ^{13}C) and 85% H_3PO_4 (^{31}P) as standards. The thermogravimetric and differential thermal analyses were performed using a PerkinElmer STA-6000 analyser under a nitrogen atmosphere at a heating rate of 5 °C/min. The DSC measurements were carried out using a Hitachi DSC200 thermal analysis system at the temperature rate of 5 °C/min. Melting point analysis was performed using a Buchi M-650 melting point apparatus. FT-IR spectra were taken on a Thermo Scientific Nicolet 6700 spectrophotometer operating in ATR mode. Variable-temperature powder X-ray diffraction data were measured in the 2θ range of 5° to 50° on a Bruker-D8 Advance X-ray diffractometer. The solid-state UV-visible spectra of **BzA·^{Cl}Ph-Cy-DMP** were measured in an optical glass cuvette at room temperature using a Shimadzu UV-3600 spectrophotometer over the range of 200-800 nm.

Synthesis of benzyl ammonium chlorophenyl dimethylcyclohexylphosphate (benzyl ammonium (4S)-4-(2-Chlorophenyl)-2-hydroxy-5,5-dimethyl-1,3,2-diaxaphosphinate 2-oxide) BzA·^{Cl}Ph-Cy-DMP: To a stirred solution of chlorophenyl dimethylcyclohexylphosphate (138.2 mg, 0.5 mmol) in a 2:1 methanol/water mixture (7.5 mL), benzylamine (54.6 µL, 0.5 mmol) was added at room temperature. The resultant solution was stirred for 1 hour, filtered through a thick pad of celite, and then left to crystallize under slow evaporation. Colorless rod-like crystals of **BzA·^{Cl}Ph-Cy-DMP** were obtained after 48 hours. Yield: 0.15 g (94.9%). M.P. 493-503 K. ^{31}P NMR (162 MHz, DMSO-d6) δ -4.82).^{1}H NMR (400 MHz, DMSO-d_6, ppm) δ 0.65(s), δ 0.92 (s), δ 3.51(dd), δ3.99 (s), δ4.06 (dd), δ5.54 (d), δ7.36 (tdd), δ7.47 (td), δ8.59 (s).^{13}C NMR (400 MHz, DMSO-d_6) δ 17.72, δ 20.46, δ 36.60, δ 42.05, δ 75.44(d), δ 78.58(d), δ126.34, δ128.11, δ128.49(d), δ128.72, δ128.99,δ130.30, δ131.67, δ134.10, δ29.66, δ136.12 FT-IR data in KBr pellet (cm^{-1}): 2958.04, 2874.53, 1624, 1595.2, 1545.82, 1462, 1583, 1278.73, 1212.42, 1054.01, 1007.95, 983.399, 937, 812.09, 750.07, 691.74 and 624.82 cm^{-1}.

Synthesis of benzyl ammonium dimethylcyclohexylphosphate (benzyl ammonium 2-hydroxy-5,5-dimethyl-1,3,2-diaxaphosphinate 2-oxide) BzA·Cy-DMP: To a stirred solution of dimethylcyclohexylphosphate (82.60 mg, 0.5 mmol) in a 2:1 methanol/water mixture (7.5 mL), benzylamine (54.6 µL, 0.5 mmol) was added at room temperature. The resultant solution was stirred for 1 hour, filtered through a thick pad of celite, and then left to crystallize under slow evaporation. Colorless rod-like crystals of **BzA·^{Cl}Ph·DMP** were obtained after 48 hours. Yield: 0.13 g (96.2%). M.P. 418-430 K. ^{31}P NMR (162 MHz, DMSO-d_6) δ -5.22).^{1}H NMR (400 MHz, DMSO-d_6, ppm) δ 0.82 (s), δ 0.88 (s), δ 1.14 (s), δ 3.63 (d), δ 3.69 (d), δ 3.99(d), δ 4.78 (s), 7.39 (m), δ 7.50 (m), δ 7.79 (dd), 8.61 (s). FT-IR data in KBr pellet (cm^{-1}): 2953.04, 2877.21, 1627.055, 1544.10, 1461.15, 1381.43, 1284.22, 1215.52, 1081.36, 1056.09, 1009.43, 988.04, 940.73, 919.35, 810.47, and 749.54 cm^{-1}.

Crystallography: Single-crystal X-ray diffraction measurements of **BzA·^{Cl}Ph-Cy-DMP** and **BzA·Cy-DMP** were carried out at different temperatures using a Bruker SMART APEX Duo diffractometer with Mo K_α radiation (λ = 0.71073Å). The crystal structures were refined by full-matrix least-squares against F^2 using all measured data with SHELXL implemented in the APEX 3 package.[1] The crystallographic refinement parameters for **BzA·Cy-DMP** at 150 K and for **BzA·^{Cl}Ph-Cy-DMP** at 150 and 297 K are summarized in Table S1. All non-hydrogen atoms were refined anisotropically, while hydrogen atoms were placed at geometrically calculated positions relative to their parent atoms. The benzyl substituent of the ammonium cation in **BzA·^{Cl}Ph-Cy-DMP** exhibits disorder at both 150 and 297 K. The atomic positions of the disordered components were modeled over two sites and refined using distance-similarity restraints and similar-displacement-parameter restraints (SAME), as implemented in SHELXL. The DIAMOND-3.1 and WinGX software packages were used to extract the bond lengths, bond angles, and structural illustrations.[2, 3]

Hirshfeld Surface Analysis: To gain insight into the non-covalent interactions in **BzA·^{Cl}Ph-Cy-DMP**, a Hirshfeld surface analysis was performed using CrystalExplorer 3.1, based on its single-crystal X-ray data.[4] This analysis enabled visualization of the various intermolecular forces at play. These intermolecular forces were indicated by different colour palettes, and the normalized contact distance (norm), shape index and curvedness were mapped onto the Hirshfeld surface of **BzA·^{Cl}Ph-Cy-DMP**. These maps provided a visual representation of the strength of intermolecular forces, such as strong (red), medium (blue), and weak (white) interactions. The dimensionless quantity (shape index) reflects the local curvature of the Hirsfeld surface, with values between 1.0 and -1.0 denoting the most convex and concave regions, respectively. For the minimal surface regions, these values were fixed to be 0. The other term, curvedness, denotes a measure of how much the shape can be curved from the Hirshfeld surface, with a general useful range of -4.0 to 0.4. Subsequently, the 2D fingerprint plot of

BzA·^{Cl}Ph-Cy-DMP can be constructed by the distance of an atom nearest to the interior (d_i) and exterior (d_e) of the generated Hirshfeld surface. The different contours (blue and grey) in the 2D fingerprint plot represent the various types of molecular interactions, specific contact information, and all contact information, based on the Hirshfeld surface. The Hirshfeld surface can be generated with an iso-value of 0.5 a.u. for the weight function.

Second Harmonic Generation (SHG) Measurements: A femtosecond laser system was employed for the Kurtz-Perry powder tests.[5] In this system, a Coherent Astrella Ti: Sapphire regenerative amplifier was employed for generating ultrashort pulses of light (800 nm, 75 fs) at a repetition rate of 1 kHz. These pulses were then fed into a wavelength-tunable Topaz Prime Vis-NIR optical parametric amplifier (, which was tuned to generate 1500 nm wavelength. The laser fluence at the sample was 0.20 mJ/cm^2 . Estimation of the relative SHG efficiency of **BzA·^{Cl}Ph-Cy-DMP** was performed using the Kurtz-Perry powder method. As an SHG reference, potassium dihydrogen phosphate (KDP) was used. **BzA·^{Cl}Ph-Cy-DMP** and KDP were separately ground and sieved through an Aldrich mini sieve set, yielding a 177−125 μm microcrystal size fraction. The sieved samples were then sealed and placed in the sample holder after being secured between microscope glass slides (creating tightly packed layers). No refractive-index-matching oil was employed. The laser beam was directed onto samples at 45° and was unfocused in all cases. Signal-collecting optics, mounted to the glass optical fibre, were placed perpendicularly to the sample plane (backscattering geometry), which was mounted on a horizontally aligned holder. The spectra of diffused SHG were recorded with an Ocean Optics Flame-T XR spectrograph. Experiment was performed at 293 K and temperature was controlled using Linkam LTS420 optical cryostat.

Ferroelectric, Piezoelectric, and Dielectric studies: The *P-E* hysteresis loop measurement was performed on the thin film of **BzA·^{Cl}Ph-Cy-DMP** using a Sawyer-Tower circuit at room temperature. The thin film was prepared by drop-casting 20 mg of **BzA·^{Cl}Ph-Cy-DMP, which** was dissolved in 0.5 ml of methanol, onto the ITO-coated glass. The colorless micrometer-sized crystallites of **BzA·^{Cl}Ph-Cy-DMP** were observed on the ITO substrate after one hour. The conductive Indium-gallium alloy was used as the electrodes. The ferroelectric measurements were performed on an aixACCT TF2000E model hysteresis loop analyser. The hysteresis loop was obtained using the double-wave method by employing the positive up and negative down (PUND) function of the instrument at 2 Hz frequency. Leakage currents were dynamically measured at various voltage steps during the hysteresis loop measurements.

The piezoelectric charge coefficient (d_{33}) of **BzA·^{Cl}Ph·DMP** was measured on a poled pellet sample (thickness of 0.62 mm, diameter of 10 mm) using the quasistatic (Berlincourt) method. The sample was corona-poled at 25 °C for 1 hour under an applied mesh voltage of 25 kV. A PM300 piezotest meter, operating with a force-frequency of 110 Hz and an amplitude of 0.25 N, was employed. The electrical contacts were made with silver conductive paste.

Temperature and frequency-dependent dielectric permittivity and dielectric loss measurements were performed on **BzA·^{Cl}Ph-Cy-DMP** pressed powder pellets. The measurements were conducted using the Solartron Analytical 1260 model Impedance Analyzer combined with a Dielectric Interface model 1296A. The sample was placed in a Janis 129610A cryostat sample holder, and a Lakeshore 336 model temperature controller was used to control the temperature.

Piezo-response force microscopy: The piezo-response force microscopy (PFM) measurements were performed on the thin film of **BzA·^{Cl}Ph-Cy-DMP** to examine its domain structure and switching dynamics. The PFM measurements were performed using the Asylum Research MFP-3D Origin+ atomic force microscopy (AFM) system. Contact mode AFM experiments were carried out using RMN-12PT300B cantilever probes, which had a spring constant of 1.12 N m^{-1} and a tip diameter of less than 8 nm, to measure the piezoresponse of the crystal films. PFM data were obtained from vertical-PFM experiments, in which an AC voltage was applied to the conductive AFM tip while the bottom electrode remained grounded. The PFM images were collected at a resonance frequency of 300 ± 20 kHz with an applied bias of 100 V. Additionally, PFM phase and amplitude contrast were recorded using dual AC resonance tracking (DART) mode.

Formation of the polymer composite film and PENG: The polymer composite film was fabricated according to a previously reported protocol as described below. Specifically, 400 mg of polycaprolactone (PCL) was dissolved in DCM at room temperature under continuous stirring. The **BzA·^{Cl}Ph-Cy-DMP** was incorporated into the solution to the desired composite weight fraction, and the mixture was thoroughly homogenized. The resulting solution was drop-cast onto a circular Petri dish and allowed to cure at room temperature for 24 h to ensure complete solvent evaporation. Subsequently, the dried polymer film was cut into 2.5 cm × 2.5 cm specimens. Copper electrodes were affixed to the opposite surfaces of the film, and electrical connections were established at the electrode terminals. The entire device was then encapsulated with Kapton tape to provide mechanical protection and electrical insulation. The energy-harvesting performance of the **BzA·^{Cl}Ph-Cy-DMP**-PCL composite devices was evaluated using a custom-built impact testing setup. Output voltage signals were measured with a Tektronix 3400 series oscilloscope operating at an input impedance of 1 MΩ.

Stress-Strain Analysis: An Intron 5943 universal testing machine was used to compare the stress-strain behaviour of pure PCL and **BzA·^{Cl}Ph-Cy-DMP**-PCL composite films on rectangular film strips with 2 mm thickness, 5mm width and 20 mm length (gauge length: 10 mm, grip length: 7.5 mm each side) at a strain rate of 5mm/min. The load cell used for testing had a capacity of 1 kN.

Fabrication of wind sensor: The contact-type wind sensor device was fabricated using a miniature wind turbine mechanically coupled to a gear–spur assembly. The gear, consisting of eight teeth, was directly connected to the turbine blades, while its other side engaged a spur wheel with twenty-four teeth, effectively reducing the rotational speed of the transmission rod. This rod was mechanically linked to a striker, which periodically passed through an accelerator mechanism and delivered controlled impacts onto the piezoelectric nanogenerator (PENG) sensor, thereby generating an electrical response. The PENG sensor was constructed from a 10 wt% **BzA·^{Cl}Ph-Cy-DMP**-PCL composite film, with thin copper sheets affixed to its opposing surfaces to serve as electrodes. Electrical connections were established via copper wires attached to the top and bottom electrodes, and the entire device was encapsulated using Kapton adhesive tape to prevent mechanical damage during operation. A plastic guiding rod was positioned adjacent to the PENG sensor to enhance the impact force by allowing the striker to partially deflect before contacting the sensor surface. The output voltage signals from the PENG sensor were transmitted to an Arduino-based microcontroller (ECU) via copper wire connections. As the fan-driven mechanical turbine operated at a constant rotational speed, the PENG sensor produced periodic voltage pulses at fixed time intervals. The microcontroller recorded the time interval between consecutive signals and computed the corresponding wind speed using the mathematical relations described in Supporting Discussion 2 (vide infra). The computational algorithm for wind-speed determination was implemented in C++ and uploaded to the microcontroller for real-time data processing.

Calibration Method: The piezoelectric wind speed sensor was calibrated using a real-time domain analysis based on the interval between consecutive electrical signal peaks. The airflow velocity was correlated with the temporal variation of the generated electrical signal, employing predefined threshold voltages to ensure accurate peak detection. Two distinct threshold levels were implemented to reliably isolate signals originating exclusively from the piezoelectric response during mechanical interaction, while effectively suppressing background noise and spurious fluctuations. A voltage threshold of 0.2 V was employed to measure low wind speeds (< 2 m s^{-1}), whereas a higher threshold of 0.3 V was applied for wind speeds exceeding 2 m s^{-1}. The 15 wt% **BzA·^{Cl}Ph-Cy-DMP**-PCL device produces a periodic voltage signal as a result of airflow-induced mechanical deformation and subsequent electromechanical conversion. A minimum threshold amplitude was applied to identify valid signal peaks, and the time interval between two successive voltage maxima (Δt) was extracted. The wind speed was calculated by using the following expressions:

$$v_{wind} = 2.0724 \times \frac{1}{\Delta t_1} \times \frac{1}{\lambda} m.s^{-1}$$

Here, Δt represents the time interval between two consecutive signals, and λ denotes the calibration factor obtained from the standard wind speed sensor. The final wind speed displayed by the sensor is the average of three simultaneous readings.

Computational studies: All computational calculations were performed using the Gaussian 09 software package.[6] The geometries of all stationary points were optimized using Density Functional Theory (DFT) at the B3LYP/6-31G(d,p) level of theory. The theoretical dipole moment calculations based on the ONIOM (Our own N-layered Integrated molecular Orbital and molecular Mechanics) approach were carried out using the group selection method, in which the anionic component was treated as the high-level layer and the cationic component as the low-level layer. The ONIOM dipole moment calculations employed the same DFT functional (B3LYP) for both layers. For the temperature-dependent strain analysis, the calculations were performed using the temperature-dependent single-crystal structure data (CIF files). Thermal corrections were applied to each temperature-specific geometry to account for the effect of temperature on molecular strain.

$$E_{angle} = \frac{1}{2} \times k_\theta (\theta_1 - \theta_0)^2$$

Where E_{angle} is the angle strain, k_θ is the angle force constant (kcal mol^{-1} rad^{-2}), θ_1 final angle, θ_0 initial angle

For strain visualization, temperature-dependent studies were carried out at 297 K, 315 K, and 333 K. The molecular geometries at each temperature were optimized using Density Functional Theory (DFT) at the B3LYP/6-31G(d) level of theory. The optimized structure at each temperature was subsequently divided into six molecular fragments for detailed strain analysis. Strain calculations were performed using the StrainViz program (available on GitHub).[7] The resulting bond, angle, and dihedral strain distributions were visualized using the Visual Molecular Dynamics (VMD) software.[8] The molecular fragments of **BzA·^{Cl}Ph-Cy-DMP**, is labelled given below as (i)–(vi). In each fragment, turquoise-coloured hydrogen atoms were added at the points of cleavage to satisfy the valency of the terminal atoms generated during fragmentation.

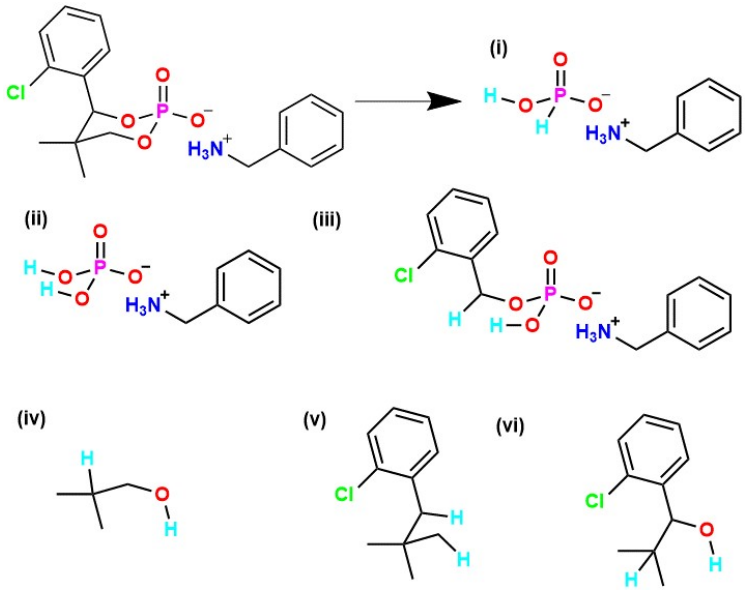

Table S1. Theoretical Mulliken charge distribution and dipole moments for the various cyclic phosphate salts with different substituted groups.

Serial Number	Compound	Mulliken charge distribution and dipole vector	Dipole moment (Debye)
1	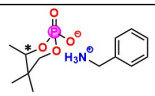	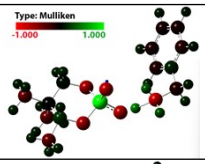	0.5362
2		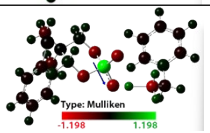	1.0045
3		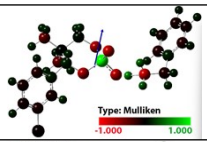	2.0854
4	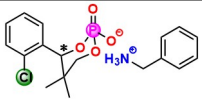	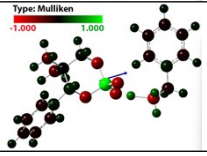	2.2399

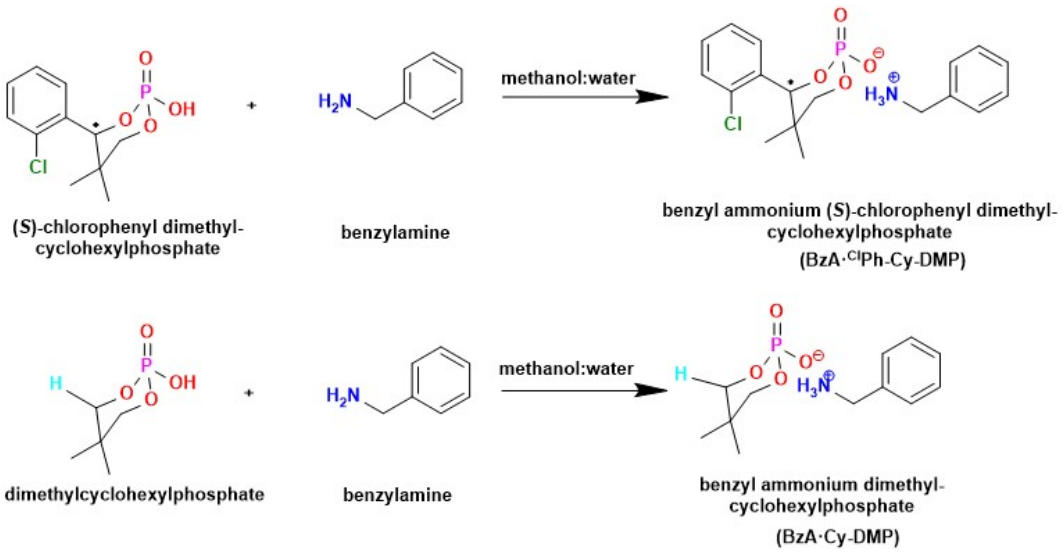

Figure S1. The schematic diagram for the synthesis of **BzA·^{Cl}Ph-Cy-DMP** and **BzA·Cy-DMP**.

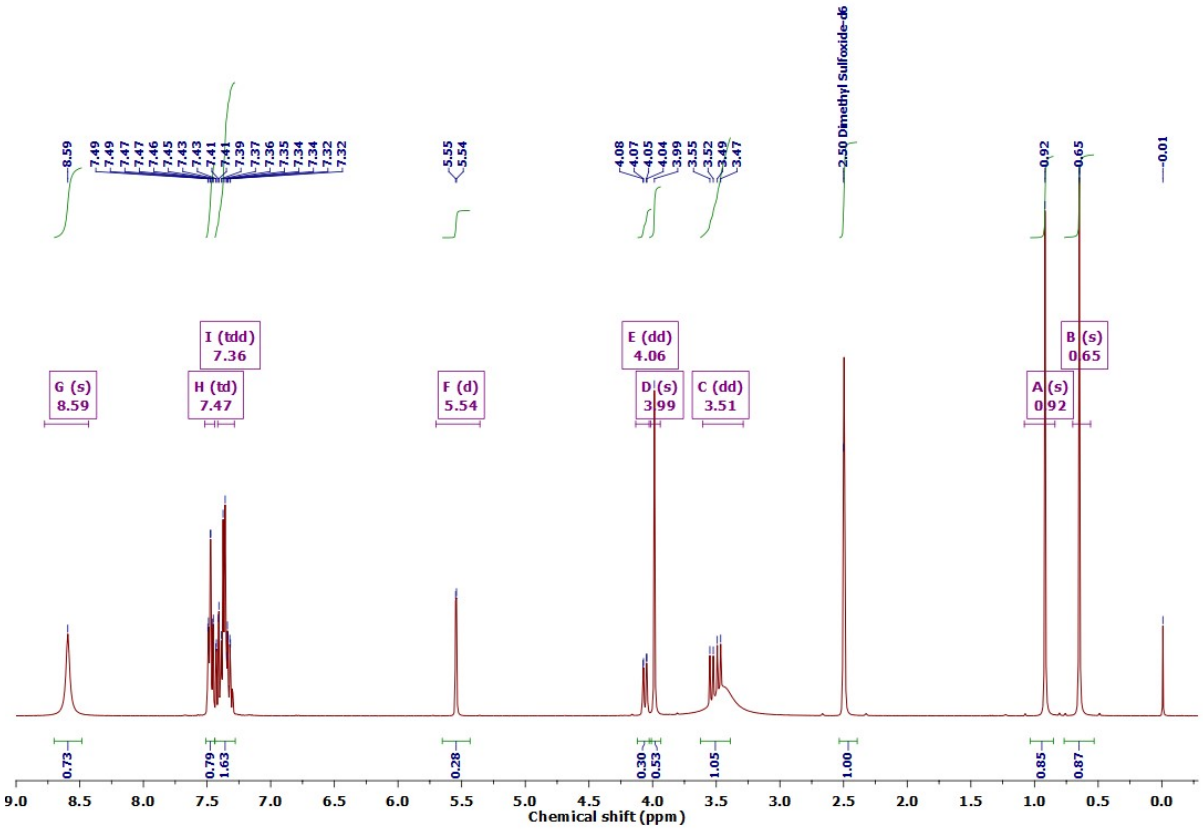

Figure S2. ^{1}H-NMR spectrum of **BzA·^{Cl}Ph-Cy-DMP** in DMSO-d_6 at 297K.

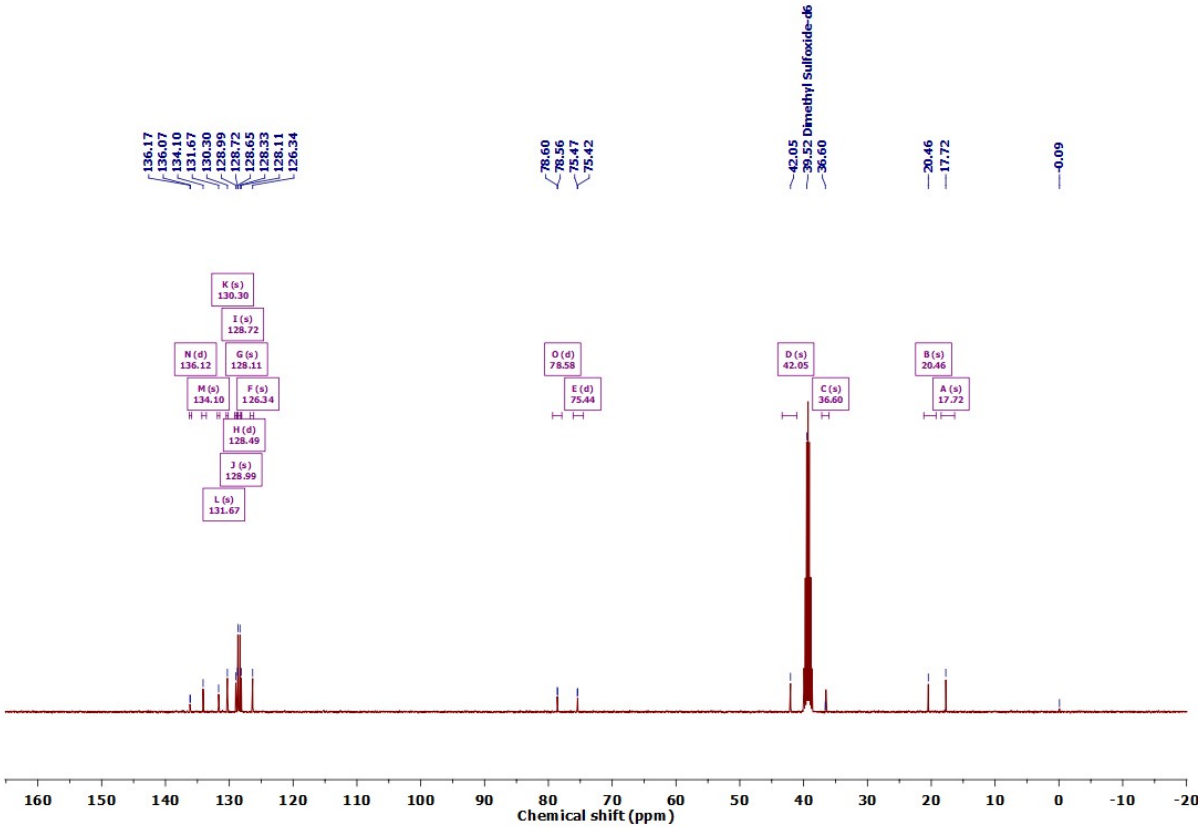

Figure S3. ^{13}C-NMR spectrum of **BzA·^{Cl}Ph-Cy-DMP** in DMSO-d_6 at 297K.

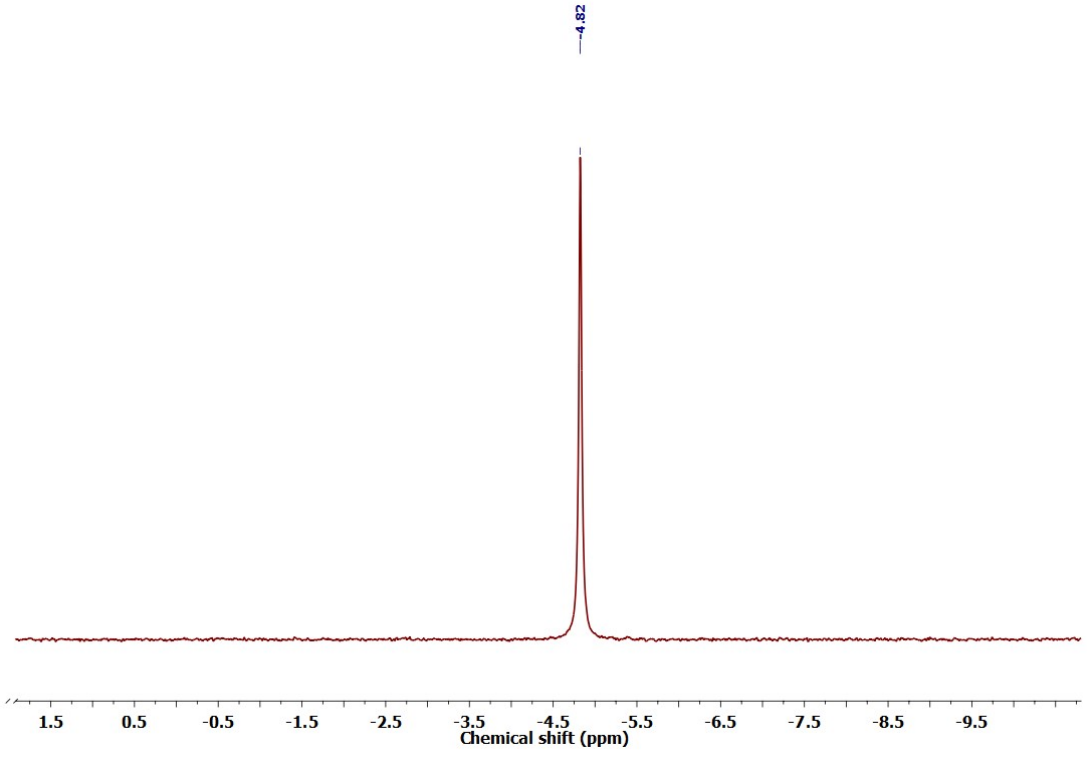

Figure S4. ^{31}P-NMR of spectra of **BzA·^{Cl}Ph-Cy-DMP** in DMSO-d_6 at 297K.

Table S2. Crystallographic data and refinement statistics of **BzA·^{Cl}Ph-Cy-DMP** at different temperatures.

Crystal data	**BzA·^{Cl}Ph-Cy-DMP**-150K	**BzA·^{Cl}Ph-Cy-DMP** 297 K	**BzA·Cy-DMP** 150 K
Chemical formula	$C_{18}H_{23}ClNO_4P$	$C_{18}H_{23}ClNO_4P$	$C_{12}H_{20}NO_4P$
Formula weight (g/mol)	383.79	383.79	273.26
Temperature (K)	150	297	150
Crystal system	Monoclinic	Monoclinic	Monoclinic
Space group	$P2_1$	$P2_1$	$P2_1/n$
a (Å); α (°)	11.383(4), 90	11.540(4), 90	5.973(3), 90
b (Å); β (°)	6.484(2), 90.367(10)	6.573(2), 90.716(10)	15.213(7), 94.219(13)
c (Å); ϒ (°)	12.571(10), 90	12.667(4), 90	15.289(7), 90
V (Å3); Z	927.9(5), 2	960.7(6), 2	1385.5(11), 4
ρ (calc.) mg m^{-3}	1.374	1.327	1.310
μ (Mo Kα) mm^{-1}	0.314	0.304	0.205
2θmax (°)	25.059	25.124	25.255
R(int)	0.0456	0.0447	0.1361
Completeness to θ	99.8 %	99.0 %	98.6 %
Data/param.	3284/ 270	3396/ 225	2474/ 178
GOF	1.051	1.034	1.035
R1 [I>2σ(I)]	0.0283	0.0307	0.0439
wR2 (all data)	0.0665	0.0787	0.1050
Flack parameter	0.05(3)	-0.01(3)	---
max. peak/hole (e.$Å^3$)	0.25/-0.19	0.17/ -0.16	0.30/ -0.32

Table S3: Selected bond lengths [Å] and angles [°] of **BzA·^{Cl}Ph-Cy-DMP** at 150 and 297 K.

Compound	**Bond length (Å)**		**Bond angle (°)**	
BzA·^{Cl}Ph-Cy-DMP (150 K)	Cl18-C18	1.745(3)	O14-P13-O12	102.30(10)
	P13-O12	1.598(2)	O15-P13-O12	109.37(11)
	P13-O14	1.596(2)	O15-P13-O14	109.48(11)
	P13-O15	1.500(2)	O15-P13-O14	109.48(12)
	P13-O16	1.481(2)	O16-P13-O12	108.69(11)
	O12-C11	1.460(3)	O16-P13-O14	108.17(12)
	O14-C9	1.453(3)	O16-P13-O15	117.72(12)
	N1-C2	1.492(4)	C11-O12-P13	115.87(16)
	C2-C3	1.487(7)	C9-O14-P13	117.19(17)
	C2-C3'	1.528(13)	N1-C2-C3'	108.5(8)
	C3-C4	1.400(8)	C3-C2-N1	112.9(4)
	C3-C8	1.379(8)	C4-C3-C2	122.9(6)
	C4-C5	1.408(7)	C8-C3-C2	118.0(6)
	C5-C6	1.378(8)	C8-C3-C4	119.1(6)
	C6-C7	1.382(8)	C3-C4-C5	121.0(6)
	C7-C8	1.375(7)	C6-C5-C4	117.7(5)
	C3'-C4'	1.355(16)	C5-C6-C7	121.6(5)
	C3'-C8'	1.417(16)	C8-C7-C6	120.1(5)
	C4'-C5'	1.374(15)	C7-C8-C3	120.5(6)

	C5'-C6'	1.392(17)	C4'-C3'-C2	117.8(11)
	C6'-C7'	1.339(17)	C4'-C3'-C8'	118.8(12)
	C7'-C8'	1.374(16)	C8'-C3'-C2	123.3(12)
	C9-C10	1.525(4)	C3'-C4'-C5'	118.0(13)
	C10-C11	1.543(4)	C4'-C5'-C6'	121.5(13)
	C10-C23	1.533(4)	C7'-C6'-C5'	122.0(13)
	C10-C24	1.529(4)	C6'-C7'-C8'	116.3(12)
	C11-C17	1.513(4)	C7'-C8'-C3'	123.0(13)
	C17-C18	1.389(4)	O14-C9-C10	112.5(2)
	C17-C22	1.394(4)	C9-C10-C11	106.9(2)
	C18-C19	1.380(4)	C9-C10-C23	109.9(2)
	C19-C20	1.382(5)	C9-C10-C24	107.1(2)
	C20-C21	1.391(5)	C23-C10-C11	112.3(2)
	C21-C22	1.382(4)	C24-C10-C11	110.6(2)
			C24-C10-C23	109.9(2)
			O12-C11-C10	108.9(2)
			O12-C11-C17	107.5(2)
			C17-C11-C10	115.2(2)
			C18-C17-C11	122.3(3)
			C18-C17-C22	117.2(3)
			C22-C17-C11	120.4(3)
			C17-C18-Cl18	120.7(2)
			C19-C18-Cl18	117.0(2)
			C19-C18-C17	122.3(3)
			C18-C19-C20	119.3(3)
			C19-C20-C21	120.1(3)
			C22-C21-C20	119.5(3)
			C21-C22-C17	121.6(3)
	Cl18- C18	1.746(4)	O14-P13-O12	102.60(11)
	P13- O12	1.600(2)	O15-P13-O12	108.80(12)
	P13-O14	1.599(2)	O15-P13-O14	108.50(15)
	P13-O15	1.478(3)	O15-P13-O16	117.92(14)
	P13-O16	1.494(2)	O16-P13-O12	109.12(12)
	O12-C11	1.454(3)	O16-P13-O14	108.81(13)
	O14-C9	1.449(4)	C11-O12-P13	116.33(16)
	N1-C2	1.489(5)	C9-O14-P13	117.01(19)

BzA·^{Cl}Ph-Cy-DMP (297 K)	C2-C3	1.452(10)	N1-C2-C3'	110.6(6)
	C2-C3'	1.533(10)	C3-C2-N1	115.6(6)
	C3-C4	1.397(12)	C4-C3-C2	125.8(9)
	C3-C8	1.362(11)	C8-C3-C2	115.7(9)
	C4-C5	1.411(14)	C8-C3-C4	118.5(9)
	C5-C6	1.337(16)	C3-C4-C5	125.3(11)
	C6-C7	1.474(13)	C6-C5-C4	112.4(12)
	C7-C8	1.366(11)	C5-C6-C7	126.1(10)
	C3'-C4'	1.365(13)	C8-C7-C6	115.9(8)
	C3'-C8'	1.397(12)	C3-C8-C7	121.7(9)
	C4'-C5'	1.366(13)	C4'-C3'-C2	115.3(8)
	C5'-C6'	1.389(17)	C4'-C3'-C8'	119.8(10)
	C6'-C7'	1.422(16)	C8'-C3'-C2	124.8(10)
	C7'-C8'	1.399(14)	C3'-C4'-C5'	121.0(11)
	C9-C10	1.526(4)	C4'-C5'-C6'	115.1(12)
	C10-C11	1.555(4)	C5'-C6'-C7'	130.1(12)
	C10-C23	1.535(4)	C8'-C7'-C6'	108.2(10)
	C10-C24	1.524(5)	C3'-C8'-C7'	125.3(11)
	C11-C17	1.525(4)	O14-C9-C10	112.9(3)
	C17-C18	1.381(5)	C9-C10-C11	106.9(2)
	C17-C22	1.394(4)	C9-C10-C23	109.7(3)
	C18-C19	1.388(5)	C23-C10-C11	112.0(3)
	C19-C20	1.370(6)	C24-C10-C9	107.3(3)
	C20-C21	1.385(6)	C24-C10-C11	110.6(3)
	C21-C22	1.387(5)	C8-C3-C2	111.7(6)
			C24-C10-C23	110.2(3)
			O12-C11-C10	109.0(2)
			O12-C11-C17	107.8(2)
			C17-C11-C10	115.3(2)
			C18-C17-C11	122.8(3)
			C18-C17-C22	117.1(3)
			C22-C17-C11	120.1(3)
			C17-C18-Cl18	120.7(2)
			C17-C18-C19	122.5(3)
			C19-C18-Cl18	116.8(3)
			C20-C19-C18	119.0(4)

			C19-C20-C21	120.5(3)
			C20-C21-C22	119.5(4)
			C21-C22-C17	121.4(3)
BzA·Cy-DMP (150 K)	P13-O12	1.5997(17)	O14-P13-O12	103.10(9)
	P13-O14	1.5954(18)	O15-P13-O12	108.13(10)
	P13-O15	1.4820(18)	O15-P13-O14	108.45(10)
	P13-O16	1.5039(18)	O15-P13-O16	118.32(10)
	O12-C11	1.458(3)	O16-P13-O12	108.00(10)
	O14-C9	1.450(3)	O16-P13-O14	109.75(10)
	C17-C10	1.529(4)	C11-O12-P13	115.66(15)
	C18-C10	1.534(3)	C9-O14-P13	116.04(15)
	N1-C2	1.492(3)	N1-C2-C3	112.9(2)
	C2-C3	1.507(3)	C4-C3-C2	120.0(2)
	C3-C4	1.393(3)	C8-C3-C2	121.3(2)
	C3-C8	1.388(3)	C8-C3-C4	118.7(2)
	C4-C5	1.387(4)	C5-C4-C3	120.3(2)
	C5-C6	1.379(4)	C6-C5-C4	120.4(3)
	C6-C7	1.382(4)	C5-C6-C7	119.6(3)
	C7-C8	1.380(3)	C8-C7-C6	120.3(3)
	C9-C10	1.527(3)	C7-C8-C3	120.8(2)
	C10-C11	1.527(3)	O14-C9-C10	111.2(2)
			C17-C10-C18	110.9(2)
			C9-C10-C17	110.0(2)
			C9-C10-C18	108.3(2)
			C9-C10-C11	108.6(2)
			C11-C10-C17	110.5(2)
			C11-C10-C18	108.4(2)
			O12-C11-C10	111.29(19)

Table S4: Mean plane deviation data for **BzA·^{Cl}Ph-Cy-DMP** and **BzA·Cy-DMP**.

T (K)	Compound	Mean plane deviation (Å)	
297	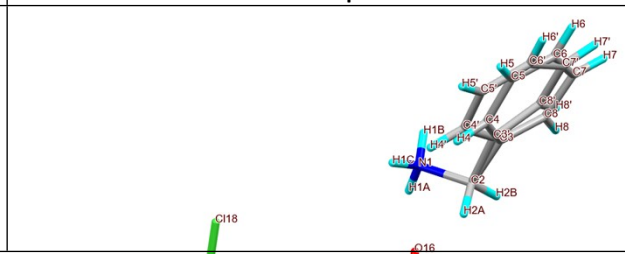	C9 = 0.238	P13 = 0.180
		H9A = 1.207	O15 = 0.677
		H9B = 0.086	O16 = 1.660
		C10 = 0.258	O14 = 0.196

		C11 = 0.284	N1 = 3.845
		H11 = 1.259	H1A = 3.205
		--	H1B = 4.610
		O12 = 0.249	H1C = 3.947
150	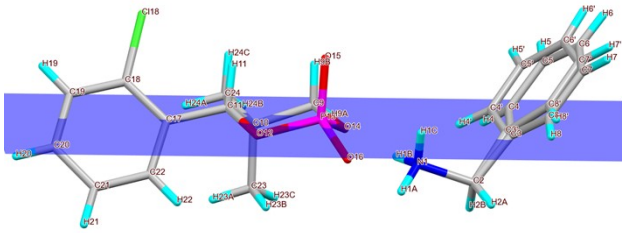 **BzA·^{Cl}Ph-Cy-DMP**	C9 = 0.236	P13 = 0.184
		H9A = 0.099	O15 = 1.670
		H9B = 1.225	O16 = 0.677
		C10 = 0.261	O14 = 0.197
		C11 = 0.288	N1 = 0.544
		H11 = 1.294	H1A = 1.154
		--	H1B = 0.448
		O12 = 0.252	H1C = 0.258
150	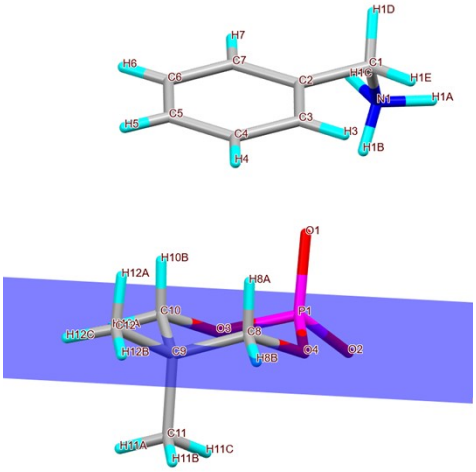 **BzA·Cy-DMP**	C9 = 0.248	P13 = 0.199
		H9A = 1.238	O15 = 0.633
		H9B = 0.074	O16 = 1.695
		C10 = 0.238	O14 = 0.229
		C11 = 0.249	N1 = 4.148
		H11A = 0.073	H1A = 0.365
		H11B = 1.239	H1B = 3.258
		O12 = 0.229	H1C = 4.148

Table S5. Hydrogen bonds and bond angles for **BzA·^{Cl}Ph-Cy-DMP** at 150 and 297 K, **BzA·Cy-DMP** at 150K.

Compound	D	H	A	d(D-H)/Å	d(H-A)/Å	d(D-A)/Å	D-H-A/°
BzA·^{Cl}Ph-Cy-DMP **(150 K)** (^{1}+X,-1+Y,+Z; ^{2}1-X,-1/2+Y,1-Z)	N1	H1A	O15^{1}	0.91	1.83	2.703 (3)	159.4
	N1	H1B	O16	0.91	1.81	2.695(3)	165.2
	N1	H1C	015^{2}	0.91	1.87	2.772(3)	173.2
BzA·^{Cl}Ph-Cy-DMP **(297 K)** (^{1}1-X,1/2+Y,1-Z; ^{2}+X,1+Y,+Z)	N1	H1A	O16	0.89	1.87	2.721(3)	158.5
	N1	H1B	O16^{1}	0.89	1.88	2.769(3)	171.9
	N1	H1C	O15^{2}	0.89	1.83	2.700(3)	165.2
BzA·Cy-DMP (150 K) (^{1}1-X,1-Y,1-Z; ^{2}-X,1-Y,1-Z)	N1	H1A	O15^{1}	1.05(3)	1.65(3)	2.688(3)	169(2)
	N1	H1B	O16	0.94(3)	1.87(3)	1.763(3)	160(3)
	N1	H1C	O16^{2}	0.97(3)	1.84(3)	2.808(3)	174(3)

Table S6: Interior and exterior angle strain around the O-P-O angle of **BzA·^{Cl}Ph-Cy-DMP** and **BzA·Cy-DMP** at 150K.

Serial	Compound	Temperature	Angle Found	Bond length	Angle Strain

No.		(K)	(°)	(°)	(kcal mol^{-1})
1	**BzA·^{Cl}Ph-Cy-DMP**	150	O-P-O$_{Interior}$ = 102.02624	1.6232	0.7986
			O-P-O $_{Exterior}$ = 116.55	1.5301	0.6359
2	**BzA·Cy-DMP**	150	O-P-O$_{Interior}$ = 101.52906	1.6254	0.2375
			O-P-O $_{Exterior}$ = 116.68214	1.5298	0.1725

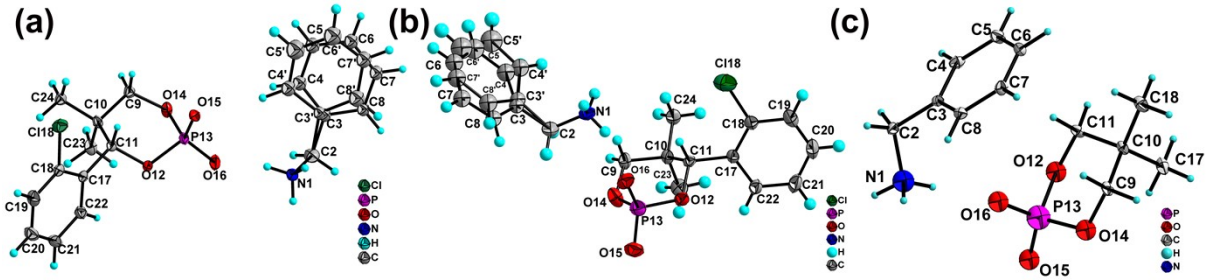

Figure S5. ORTEP-style representations of the asymmetric units of (a) **BzA·^{Cl}Ph-Cy-DMP** at 150 K. (b) **BzA·^{Cl}Ph-Cy-DMP** at 297 K. (c) **BzA·Cy-DMP** at 150 K, with thermal ellipsoids drawn at the 50% probability level.

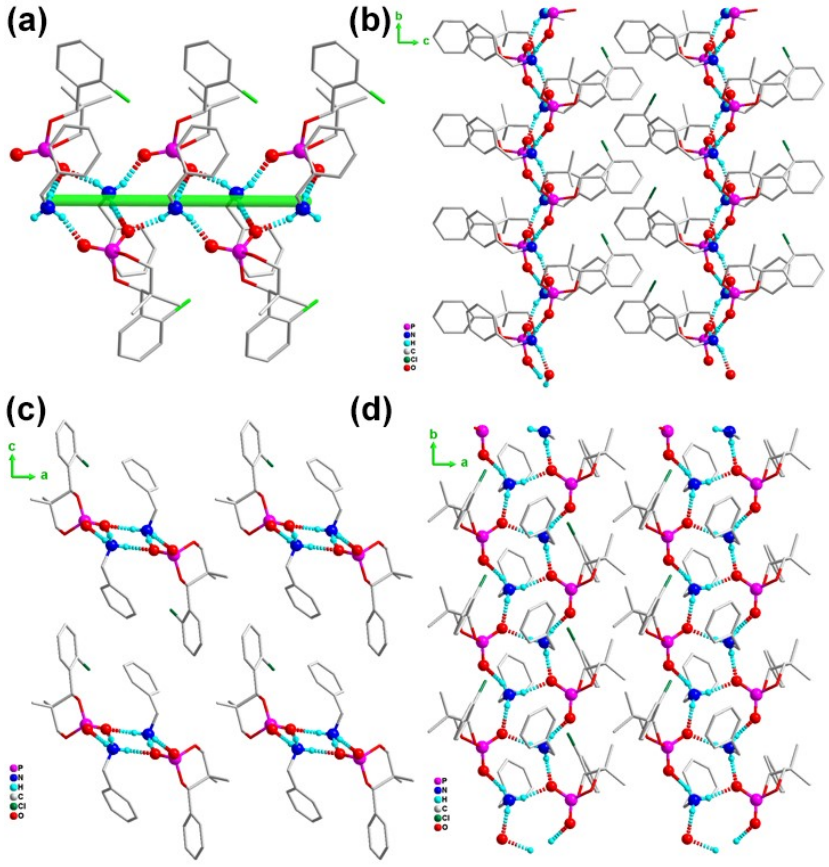

Figure S6: (a) View of the H-bonded 1D-helical structure of **BzA·^{Cl}Ph-Cy-DMP** along the *b*-axis. H-bonded packing diagram of **BzA·^{Cl}Ph-Cy-DMP** (b) along *a*-axis, (c) *b*-axis, and (d) *c*-axis.

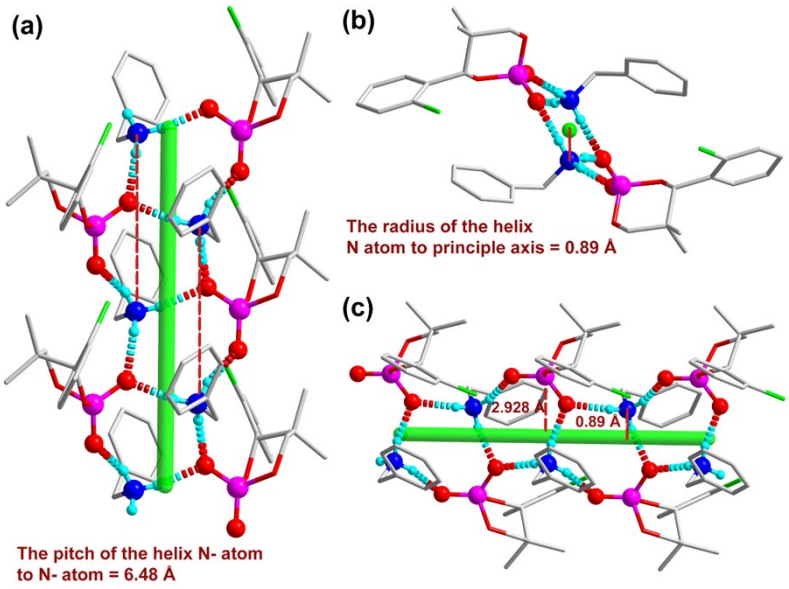

Figure S7: The structure of **BzA·^{Cl}Ph-Cy-DMP** adopts a helical arrangement along the b-axis, forming a ladder-like configuration. (a) The pitch of the helix is determined from P-atom to P-atom. (b) The radius of the helix measured from the principal axis to the nitrogen atom. (c)The radius of the helix measured from the principal axis to the phosphorous atom.

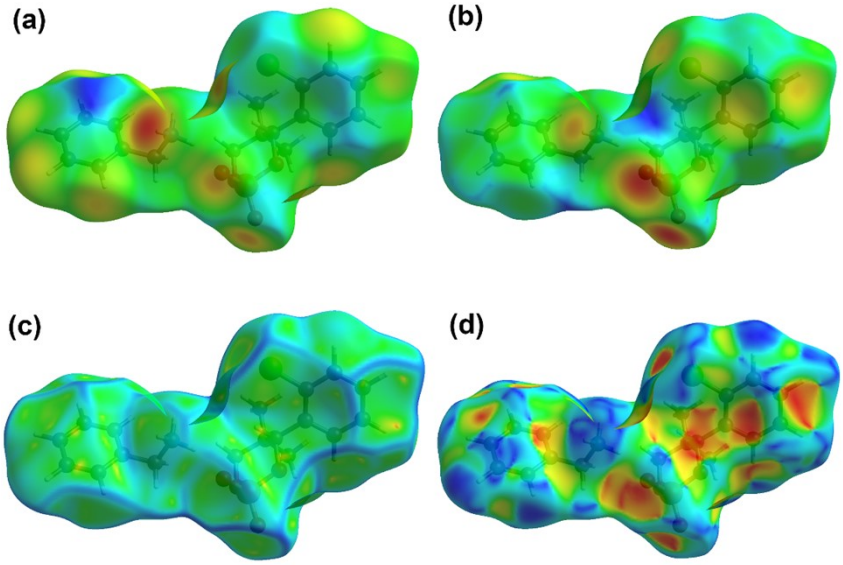

Figure S8. The 3D colour mapping obtained from the Hirshfeld surface analysis of **BzA·^{Cl}Ph-Cy-DMP** at 297 K illustrating (a) d_i, (b) d_e, (c) curvedness, and (d) shape index.

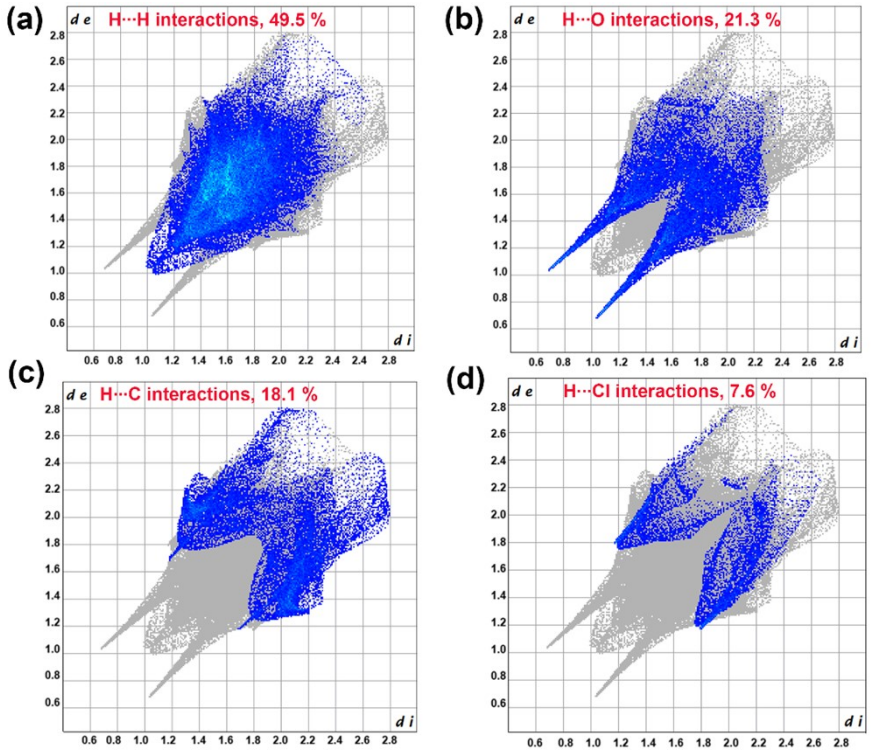

Figure S9. 2D fingerprint (d_e vs. d_i) plots of **BzA·^{Cl}Ph-Cy-DMP** (297 K) showing the percentages of (a) H···H, (b) O···H/H···O, (c) H···C/C···H, (d) Cl···H/H···Cl interactions.

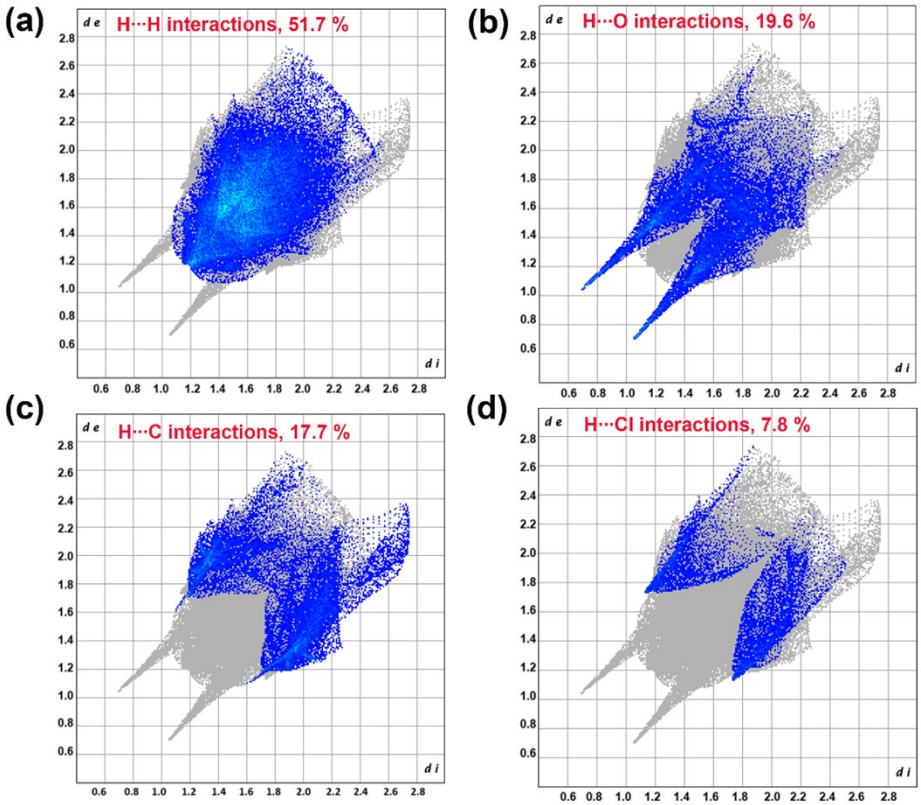

Figure S10. 2D fingerprint (d_e vs. d_i) plots of **BzA·^{Cl}Ph-Cy-DMP** (150 K) showing the percentages of (a) H···H, (b) O···H/H···O, (c) H···C/C···H, (d) Cl···H/H···Cl interactions.

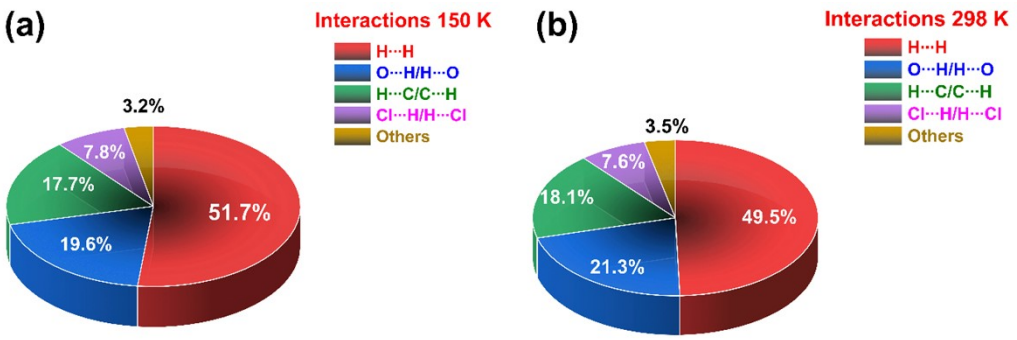

Figure S11. 3D-Pie graph of all types of percentage Interactions present in **BzA·^{Cl}Ph-Cy-DMP** at (a) 150 K and (b) 297 K.

Table S7. Hirshfeld surface analysis of **BzA·^{Cl}Ph-Cy-DMP** at 150 K and 297 K.

Compound	Temp. (K)	Surface Property	Range (minimum/maximum)	Globularity and Asphericity	Surface Volume and Area
BzA·^{Cl}Ph-Cy-DMP	**150**	d_i	0.6988/2.7587	0.705 and 0.319	455.67 Å^3 and 406.21 Å^2
		d_e	0.699/2.7536		
		d_{norm}	-0.6673/1.5335		
		Curvedness	-3.5793/0.4378		
		Shape Index	-0.9974/0.9977		
BzA·^{Cl}Ph-Cy-DMP	**297**	d_i	0.6826/2.8129	0.725 and 0.282	472.28 Å^3 and 404.70 Å^2
		d_e	0.6829/2.8144		
		d_{norm}	-0.6172/1.5984		
		Curvedness	-3.9669/0.4999		
		Shape Index	-0.9985/0.9992		

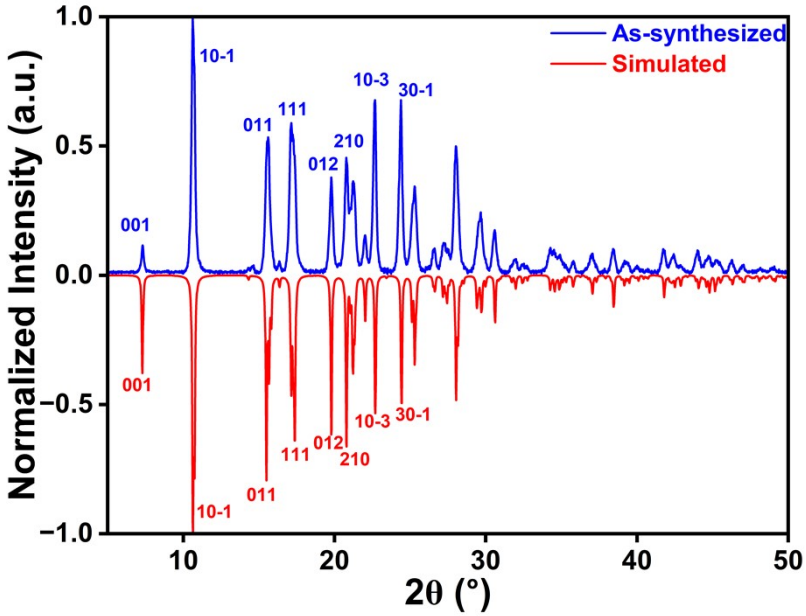

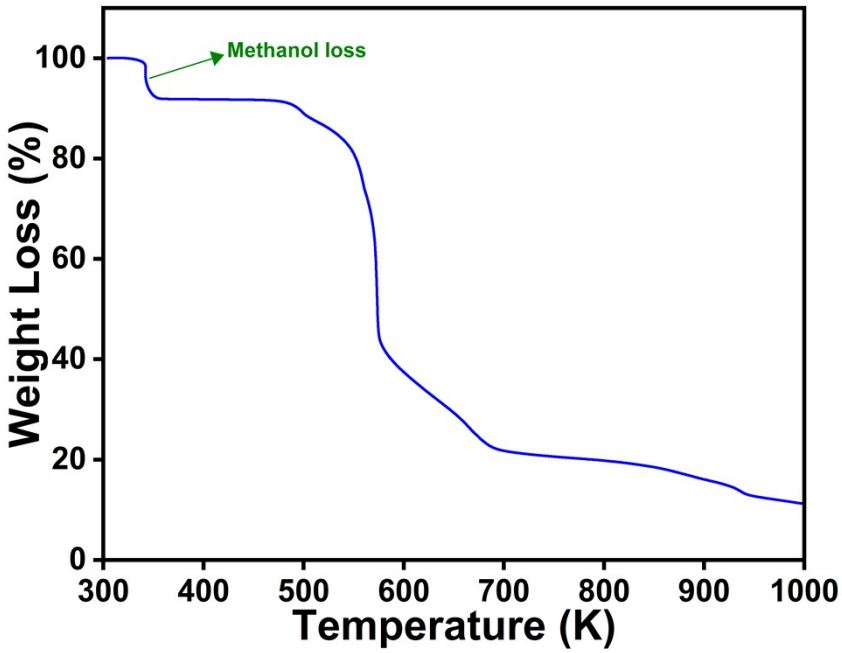

Figure S12. The PXRD profiles of simulated and as-synthesized **BzA·^{Cl}Ph-Cy-DMP**.

Figure S13. TGA profile of **BzA·^{Cl}Ph-Cy-DMP**.

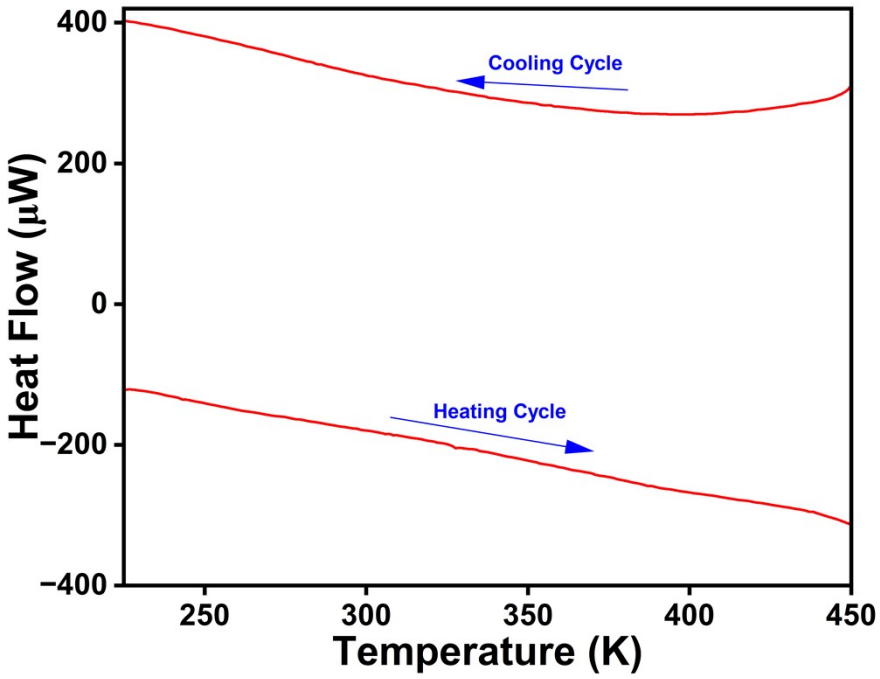

Figure S14. Differential scanning calorimetry (DSC) profiles of **BzA·^{Cl}Ph-Cy-DMP**.

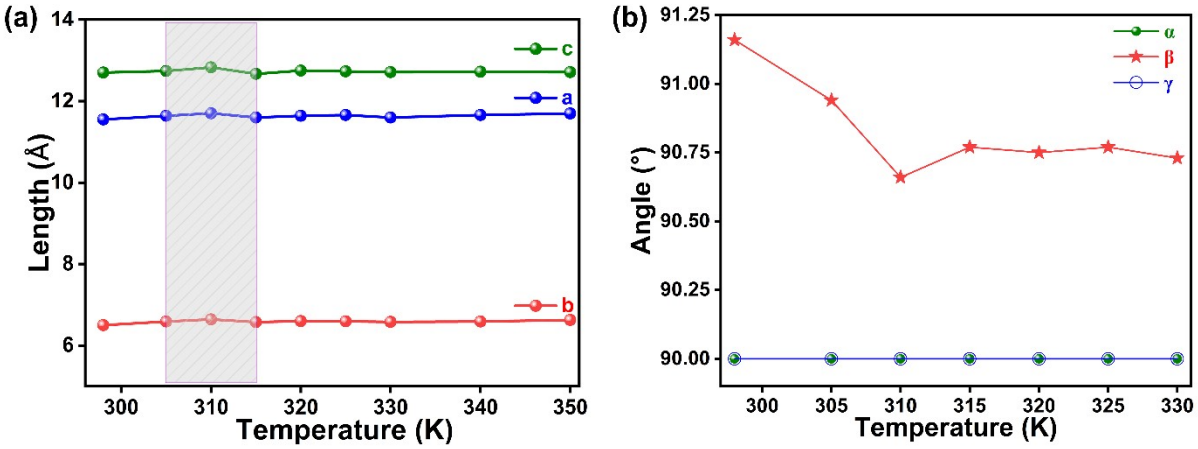

Figure S15. Variable temperature SCXRD-derived unit cell parameters for **BzA·^{Cl}Ph-Cy-DMP**.

(a) Unit cell lengths (a, b, c) and (b) angles (α, β, γ).

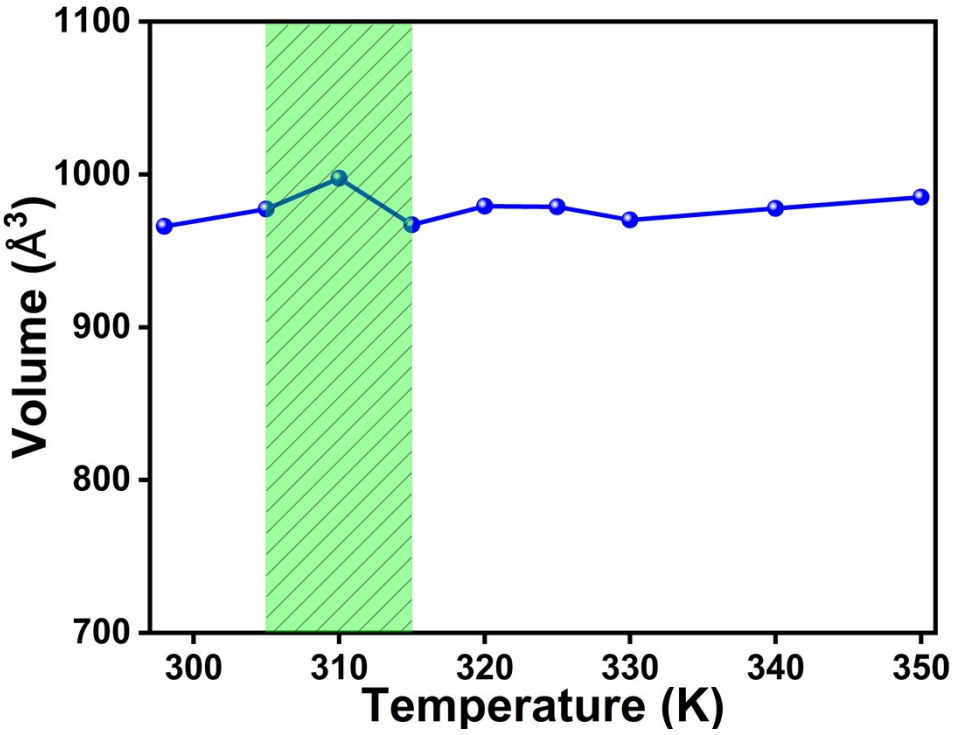

Figure S16. Variable temperature SCXRD-derived unit cell volume for **BzA·^{Cl}Ph-Cy-DMP**.

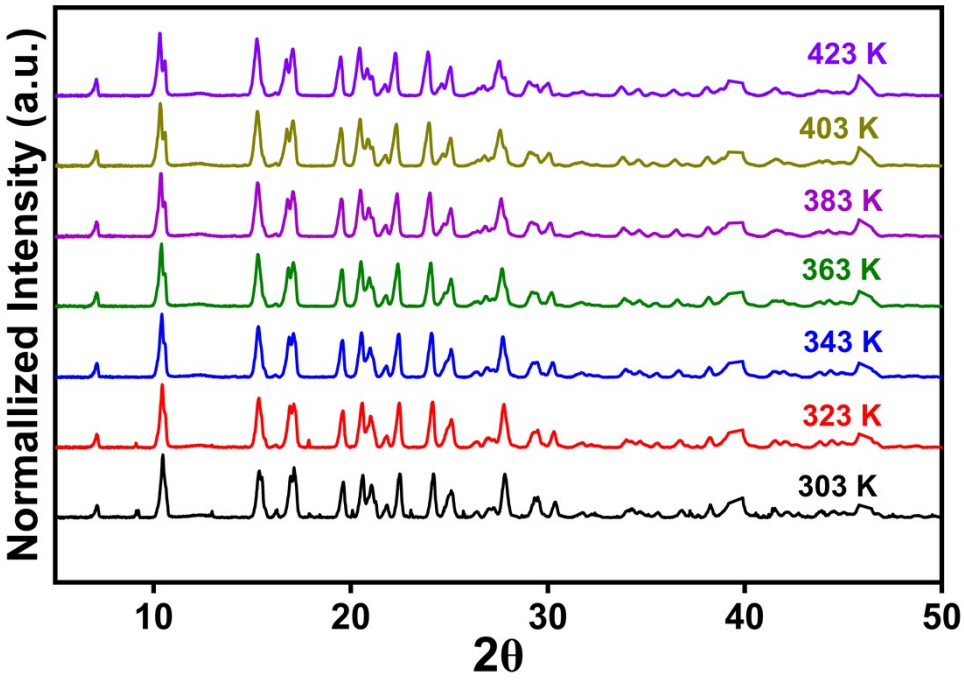

Figure S17. The variable-temperature PXRD data of **BzA·^{Cl}Ph-Cy-DMP**.

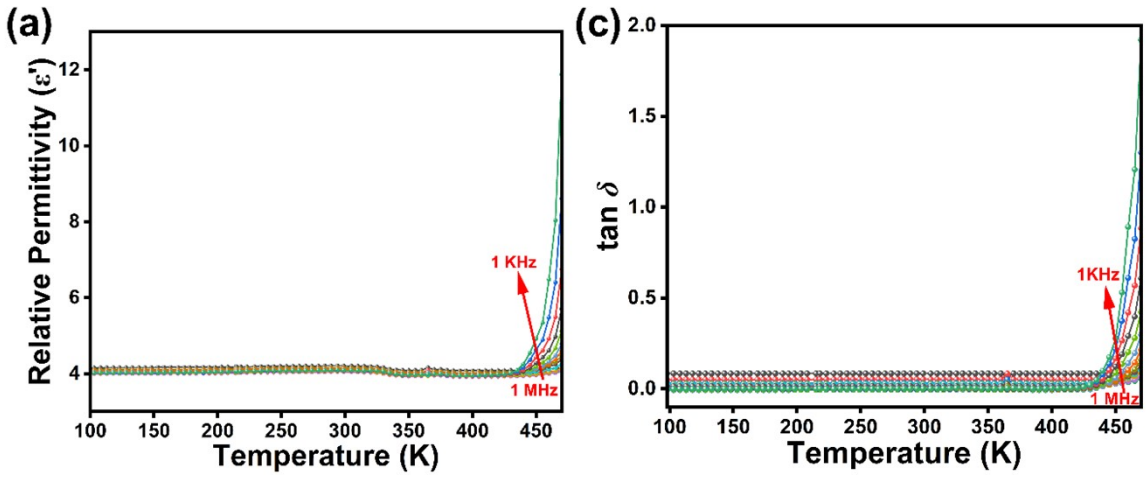

Figure S18. (a) The real part of dielectric permittivity versus temperature profile of **BzA·^{Cl}Ph-Cy-DMP**. (b) The dielectric loss factor (tan δ) versus temperature profile of **BzA·^{Cl}Ph-Cy-DMP**.

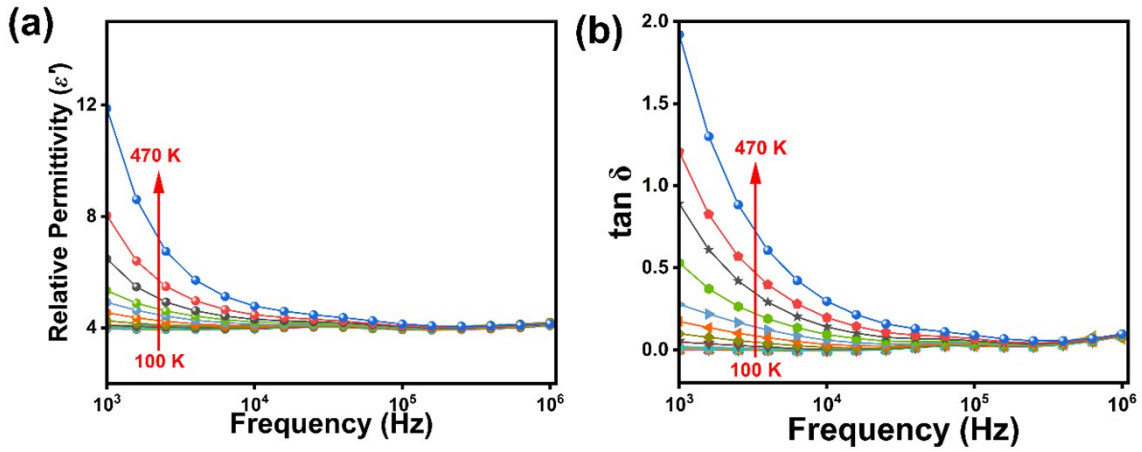

Figure S19. (a) Dielectric permittivity versus frequency profile of **BzA·^{Cl}Ph-Cy-DMP** at various temperatures. (b) Dielectric loss factor (tan δ) versus frequency profile of **BzA·^{Cl}Ph-Cy-DMP** at various temperatures.

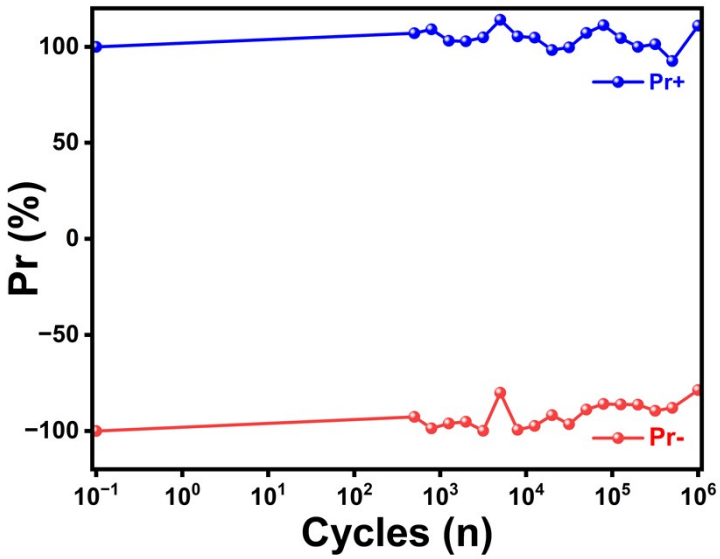

Figure S20. Ferroelectric Fatigue profile data of **BzA·^{Cl}Ph-Cy-DMP** up to 10^6 cycles.

Piezoelectric Test Report

5th Aug 2025

Sample Shape: Disc

Outer Ø 10
Thickness, t 1.41

No.	Date	Time	Freq	$F_{dyn.}$	$F_{stat.}$	Rng	d_{33}	C	tan δ	$\varepsilon_r^t{}_{33}$	g_{33}	Sens
	YYYY-MM-DD	HH:MM:SS	Hz	N	N		pC/N	pF			mV/m/N	dB
1	2025-08-05	10:00:43	110	0.25	0.1	VLO	8.35	2083	0.0036	4224	0.223	-250.0
2	2025-08-05	10:00:46	110	0.25	0.1	VLO	8.35	2083	0.0036	4224	0.223	-250.0
3	2025-08-05	10:00:53	110	0.25	0.1	VLO	8.35	2083	0.0036	4224	0.223	-250.0
4	2025-08-05	10:01:38	110	0.25	0.1	VLO	8.35	2083	0.0036	4224	0.223	-250.0
5	2025-08-05	10:01:42	110	0.25	0.1	VLO	8.35	2083	0.0036	4224	0.223	-250.0

Statistical Analysis

Mean Value	$\bar{d}_{33} = 8.351 \pm 0.000$ pC/N	$\bar{C} = 2083.1 \pm 0.0$ pF	$\bar{g}_{33} = 0.22 \pm 0.00$ mV/m/N
Standard Deviation	$\sigma_d = 0.0000$ pC/N	$\sigma_C = 0.00$ pF	$\sigma_g = 0.000$ mV/m/N
Number of Samples	$N_d = 5$	$N_C = 5$	$N_g = 5$

Figure S21. The d_{33} values for a compacted pellet of **BzA·^{Cl}Ph-Cy-DMP**.

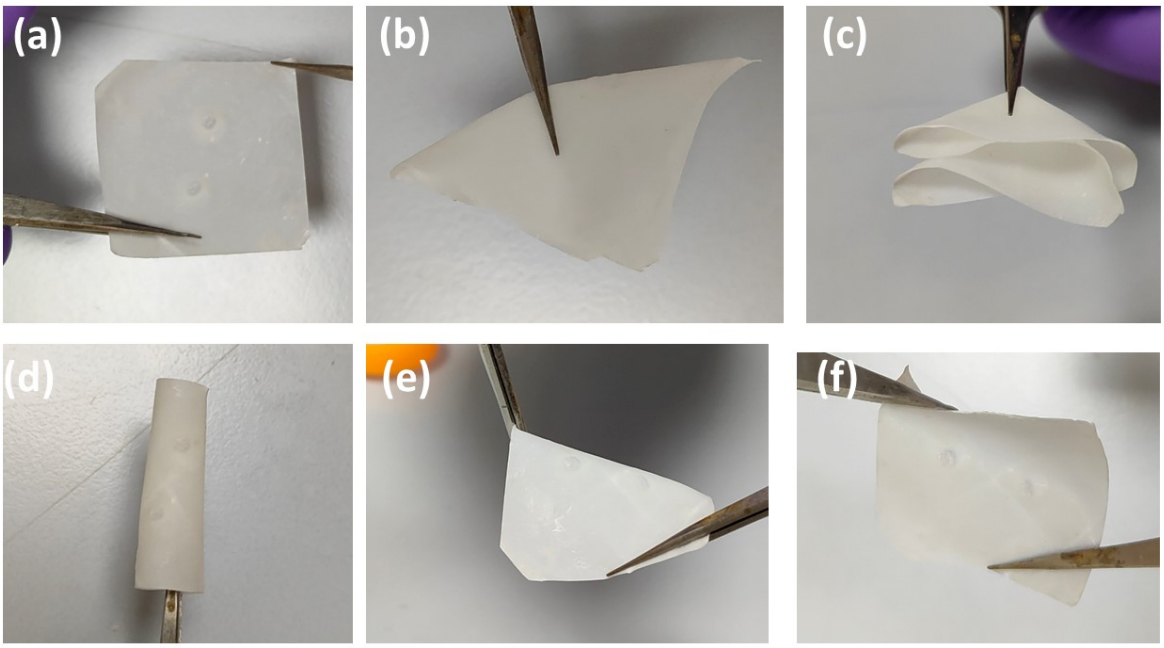

Figure S22. Photograph of a representative (a) as-made composite film of **BzA·^{Cl}Ph-Cy-DMP**-PCL showing its flexibility towards (b) Two-fold bending, (c) Four-fold folding, (d) Rolling, (e) Diagonal stretching, (f) Twisting operations.

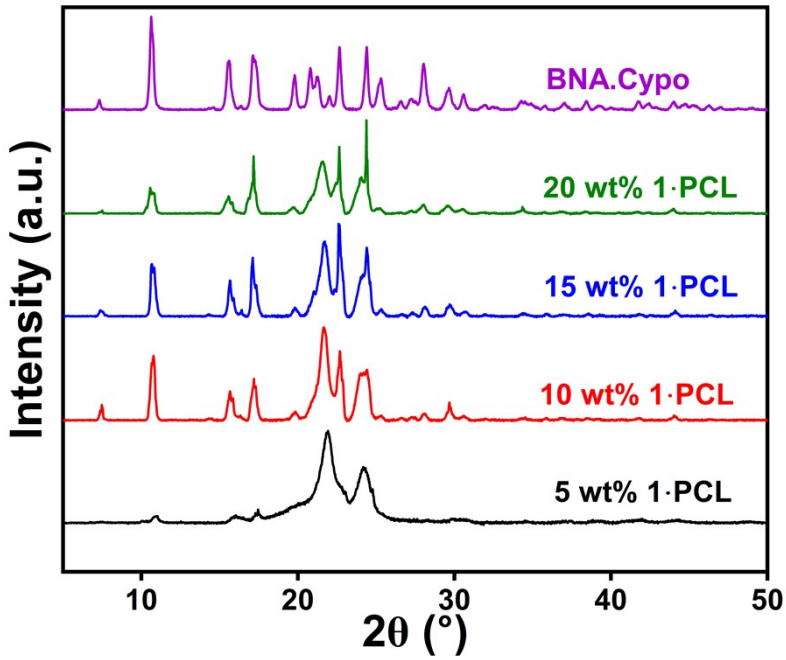

Figure S23. PXRD profiles of various weight percentage (5 wt%, 10 wt%, 15 wt%, 20 wt%) **BzA·^{Cl}Ph-Cy-DMP**-PCL composite films, and their comparison with pristine **BzA·^{Cl}Ph-Cy-DMP**.

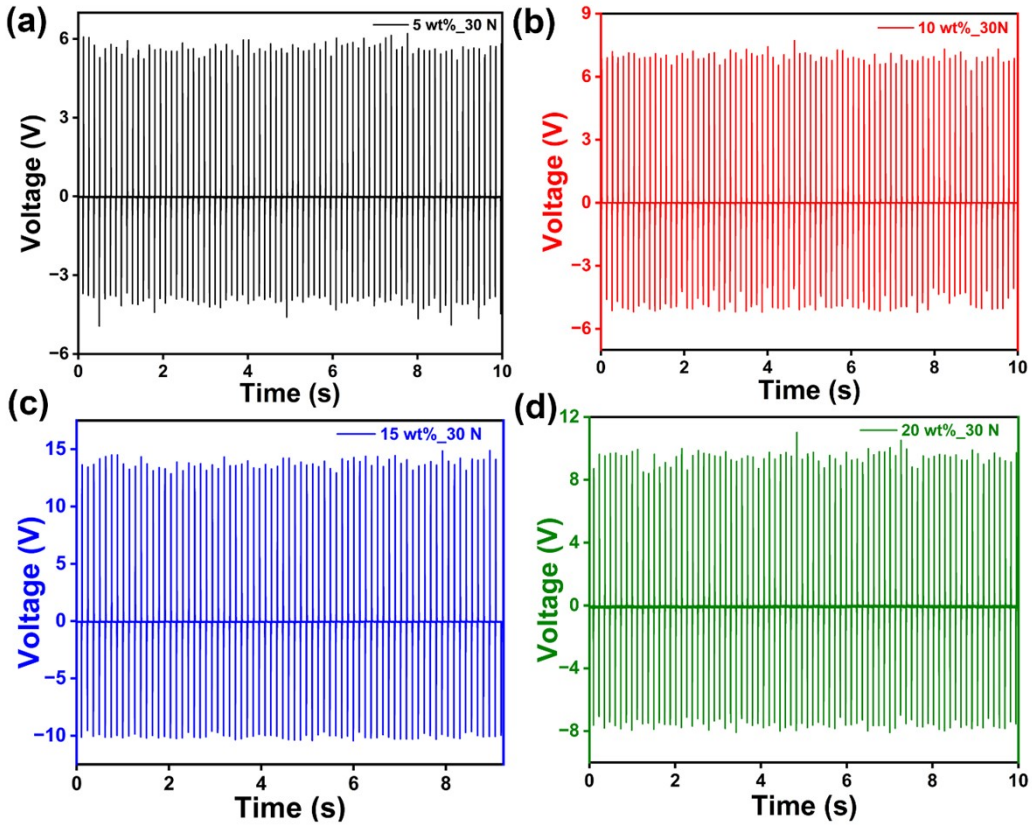

Figure S24. The piezoelectric output, open-circuit voltages of the various wt% of **BzA·^{Cl}Ph-Cy-DMP**-PCL PENG devices (a) 5 wt% (b) 10 wt% (c) 15 wt% (d) 20 wt%.

Table S8: The peak-to-peak output voltage for devices with different **BzA·^{Cl}Ph-Cy-DMP**–PCL weight percentages, along with the corresponding standard deviations.

Sr. No.	Different weight % of **BzA·^{Cl}Ph-Cy-DMP**-PCL device	Output voltage (V_{pp}) at 30 N	Standard deviation (S_d)	Output voltage (V_{pp}) at 30 N
1	5 wt%	9.562	0.115	9.58±0.115
		9.710		
		9.484		
2	10 wt%	11.736	0.135	11.87±0.135
		12.006		
		11.877		
3	15 wt%	23.597	0.022	23.60±0.022
		23.632		
		23.579		
4	20 wt%	17.102	0.143	16.90±0.143
		16.843		
		16.904		

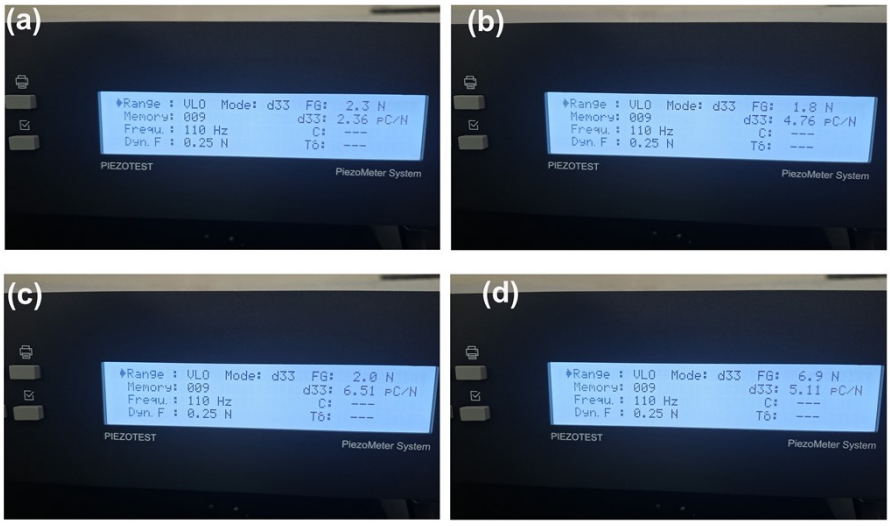

Figure S25. Photographs of the d_{33} meter showing the direct piezoelectric coefficients (d_{33}) of the poled (a) 5 wt%, (b) 10 wt%, (c) 15 wt%, and 20 wt% of **BzA·^{Cl}Ph-Cy-DMP**-PCL composite films.

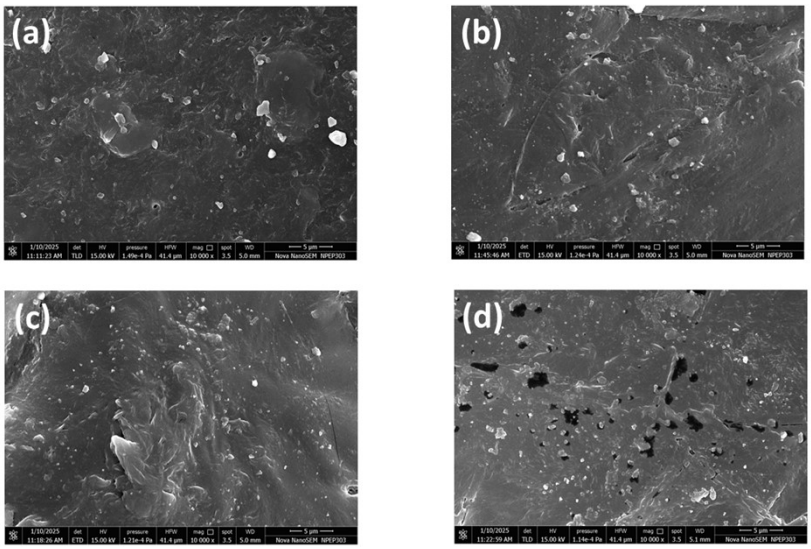

Figure S26. (a**)** The FE-SEM images of (a) 5 wt% (b) 10 wt% (c) 15 wt% (d) 20 wt% **BzA·^{Cl}Ph-Cy-DMP**-PCL composite films.

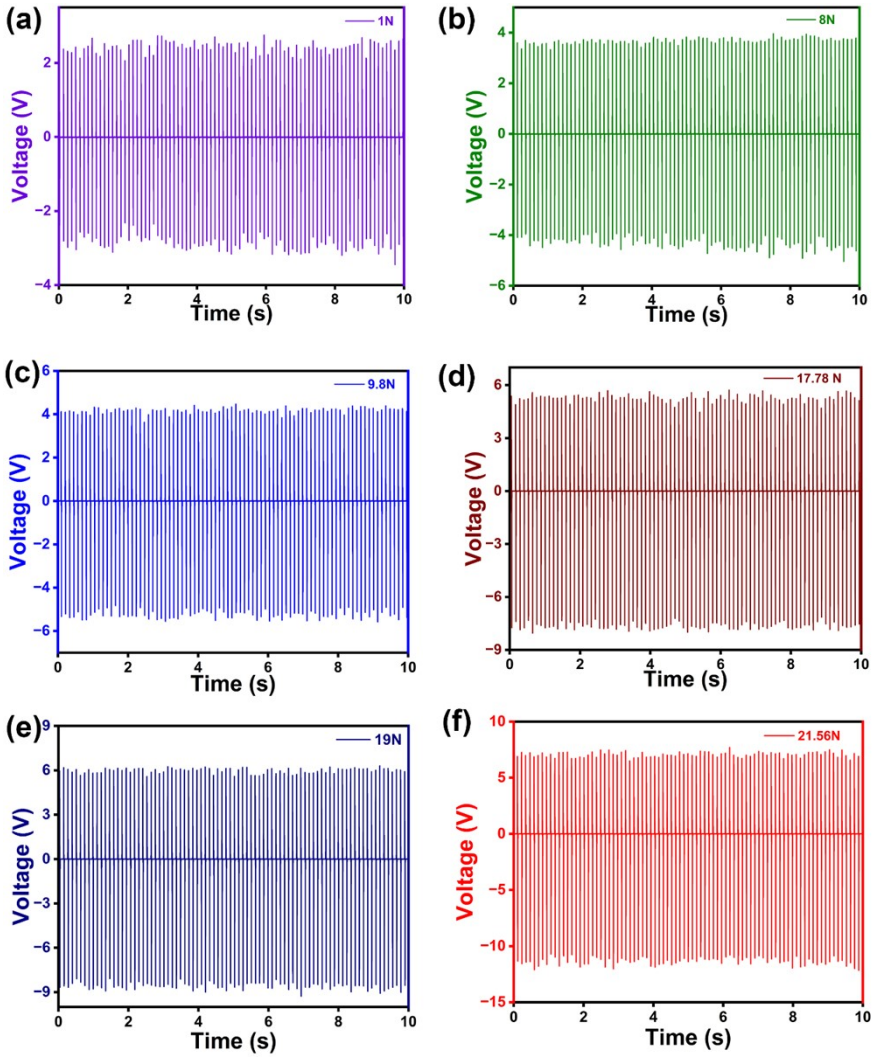

Figure S27. Force-dependent piezoelectric open circuit output voltage of 15 wt% **BzA·^{Cl}Ph-Cy-DMP**-PCl device measured at applied force loads of (a) 1 N (b) 8 N (c) 9.8 N, (d) 17.8 N and (e) 21.56 N.

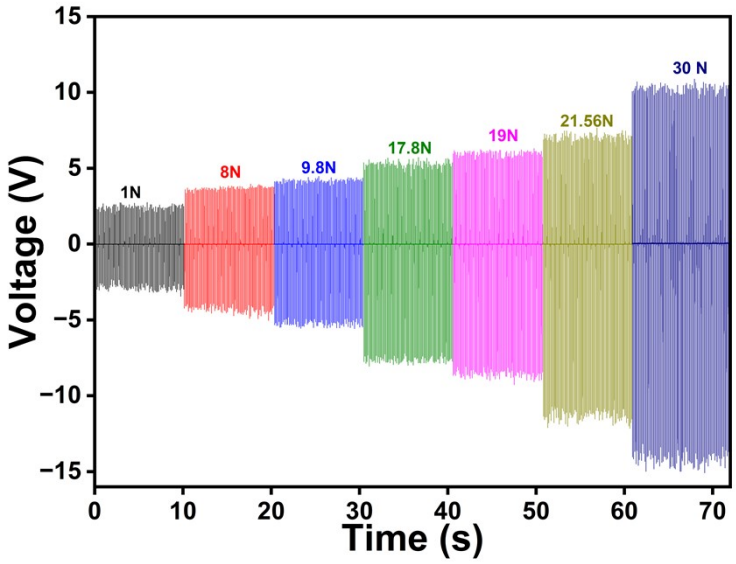

Figure S28. Comparative force-dependent piezoelectric open circuit output voltages of 15 wt% **BzA·^{Cl}Ph-Cy-DMP**-PCL. device.

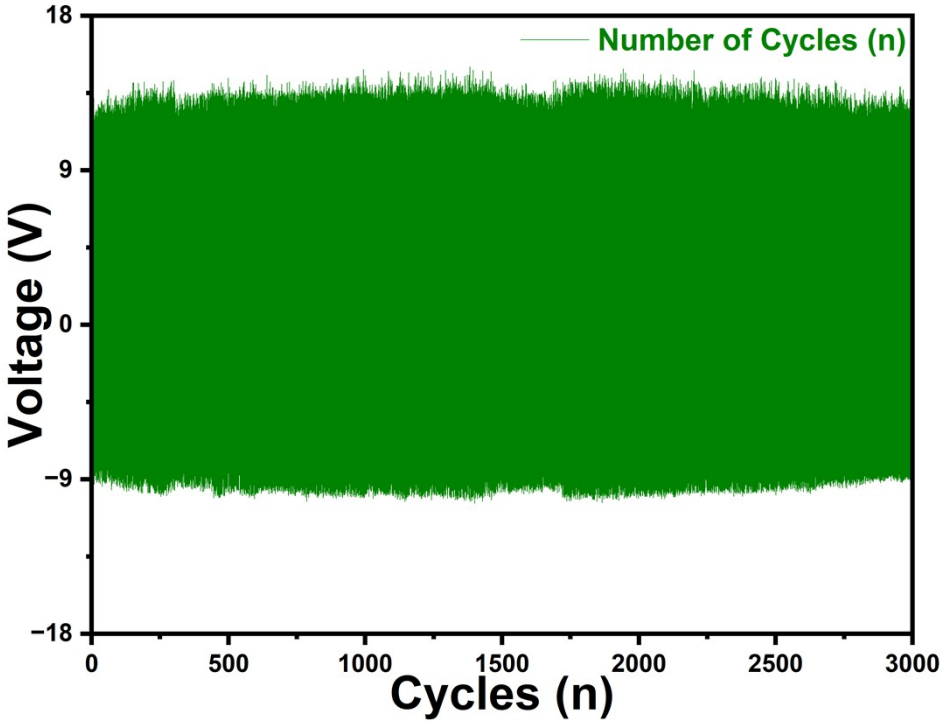

Figure S29. Cyclic stability of 15 wt% of **BzA·^{Cl}Ph-Cy-DMP**-PCL device under the force of 30 N.

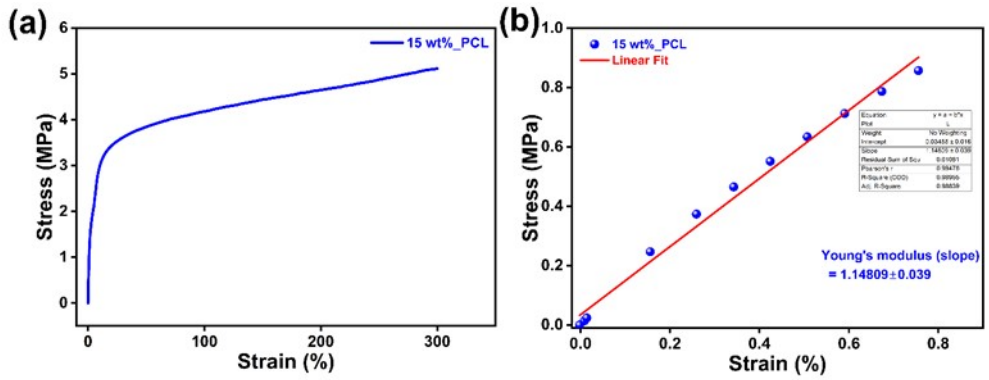

Figure S30. (a) Stress-Strain viscoelastic measurement of the 15 wt% **BzA·^{Cl}Ph-Cy-DMP**-PCL composite film up to 300% strain. (b) Fitted stress-stain plot for the 15 wt% % **BzA·^{Cl}Ph-Cy-DMP**-PCL in the linear region at ultra-low strain percentages.

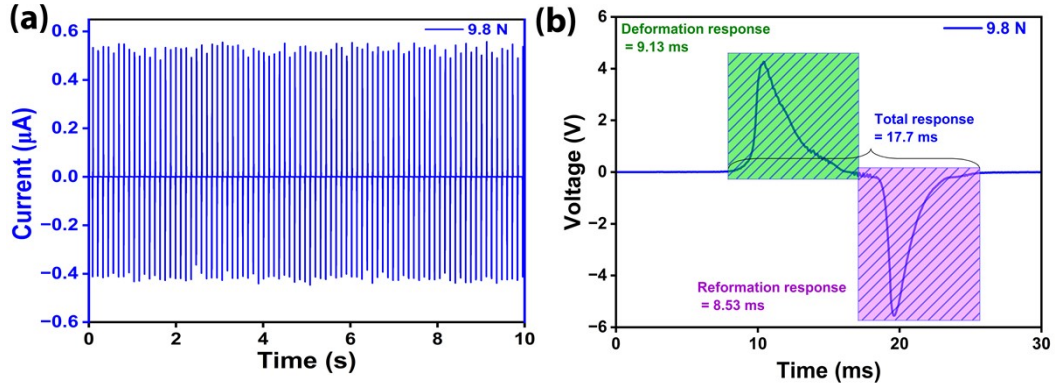

Figure S31. Pressure sensing characteristics of the 15 wt% **BzA·^{Cl}Ph-Cy-DMP**-PCL PENG device under a load of 9.8 N. (a) Open circuit current of 15 wt% **BzA·^{Cl}Ph-Cy-DMP**-PCL device (b) Enlarged large view for once cycle of positive and negative signal time intervals for the output voltages.

Supporting Discussion 1: Device Efficiency/ Work efficiency calculation:

To assess the efficiency of the 15 wt% **BzA·ClPh-Cy-DMP**-PCL-based piezoelectric nanogenerator (PENG), we determined its output work efficiency (OWE) using the protocol we previously developed.[9] The OWE was defined as the ratio of the device's output electrical energy per unit time to the intrinsic elastic (mechanical strain) energy stored in the 15 wt% **BzA·^{Cl}Ph-Cy-DMP** composite film per unit time.

The intrinsic elastic deformation energy (U_d) is given by

$$U_d = \frac{1}{2} \times \frac{stress^2}{Young's\ modulus} \times volume\ of\ effective\ area \quad \rightarrow \text{Eqn. 1}$$

Here, an external force of 9.8 N was applied to the device, which possesses an effective active surface area of 6.25 cm². The device film exhibits a uniform thickness of 0.43 mm. The resulting applied pressure, calculated as the ratio of force to unit area, corresponds to an applied stress of 0.0157 MPa on the 15 wt% **BzA·^{Cl}Ph-Cy-DMP** device. From the stress–strain response (Figure S27b), the corresponding Young's modulus of the composite was determined to be 1.1480 MPa.

$$U_d = \frac{1}{2} \times \frac{(0.0157\ MPa)^2}{1.1480\ MPa} \times (6.25\ cm^2 \times 0.0430\ cm)$$

$$U_d = \frac{1}{2} \times (0.0157)^2 \times 10^6\ N/m^2 \times \frac{1}{1.1480} \times (0.26875\ cm^3)$$

$$U_d = \frac{1}{2} \times (0.0157)^2 \times 10^6\, N/m^2 \times \frac{1}{1.1480} \times (0.26875 \times 10^{-6}\, m^3)$$

$$U_d = 1.1541 \times 10^{-4}\, N.m$$

$$U_d = 1.1541 \times 10^{-4}\, J \quad \rightarrow \text{Eqn. 2}$$

The deformation energy per second by the device can be expressed as input work done (W_d) per second, as shown below.

$$W_d = \frac{U_d}{s_d} J/s \quad \rightarrow \text{Eqn. 3}$$

Where s_d is the deformation time for the composite film, which can be calculated as given below.

The frequency of the applied impact force from the custom-built setup was maintained at 8 Hz, corresponding to a total cycle time of 125 ms (1/8 s) for one complete deformation–reformation process of the composite. Within this cycle, the 15 wt% **BzA·^{Cl}Ph-Cy-DMP** device was observed to generate one complete set of peak-to-peak output voltages over a duration of 17.66 ms. Of this interval, the positive half-cycle lasted 9.13 ms, which corresponds to the deformation stage of the device. By considering the ratio between the measured deformation time and the total signal duration (deformation + reformation + delay, with the delay assumed to be zero) corresponding to one complete positive–negative cycle of output signals from the 15 wt% **BzA·^{Cl}Ph-Cy-DMP** device, and equating this ratio to the deformation fraction within the full mechanical cycle of the impact force setup (125 ms at 8 Hz), the accurate deformation time (s_d) for one complete cycle can be determined as follows:

$$s_d = \frac{9.13\, ms}{17.66\, ms} \times\ 125\, ms$$

$$s_d = 64.62\ \times\ 10^{-3}\, s \quad \rightarrow \text{Eqn. 4}$$

Substituting the value of $U_d$from Eqn. 2 and the value of s_d from Eqn. 4 in Eqn. 3, we get the input work done (W_d) per second as below

$$W_d = \frac{1.1541\ \times 10^{-4}}{64.62\ \times\ 10^{-3}} Js^{-1}$$

$$W_d = \ 1.79 \times\ 10^{-3} Js^{-1} \quad \rightarrow \text{Eqn. 5}$$

Similarly, the output electrical energy (U_e) can be obtained from the output voltage and calculated current of the device in unit time

$$U_e = V \times i \times t \quad \rightarrow \text{Eqn. 6}$$

From the output profile shown in Figure S28b, the total duration of one complete cycle of peak-to-peak voltage oscillation (including both positive and negative half-cycles) was determined to be 17.66 ms. Within this cycle, the maximum peak-to-peak output voltage reached 9.65 V, while the corresponding current was calculated to be 0.95 µA. The internal resistor of the digital multimeter was 10 MΩ. The output electrical energy (U_e) generated per unit time (e.g., in 1 ms) can be expressed as

$$U_e = 9.65\, V \times (0.95 \times 10^{-6}\, A) \times \left(\frac{1}{17.66}\right) ms$$

Converting the time to the SI unit (s), U_e can be given by

$$U_e = 9.65\, V \times (0.95 \times 10^{-6}\, A) \times \left(\frac{1}{17.66 \times 10^{-3}}\right) s$$

$$U_e = 9.65\, V \times \left(0.95 \times 10^{-6}\, A\right)\left(\frac{1}{17.66} \times 1000\right) s$$

$$U_e = 9.65\,V \times (0.95 \times 10^{-6})\,C/s \times (56.63\,s)$$

$$U_e = 5.19 \times 10^{-4}\,V.C$$

$$U_e = 5.19 \times 10^{-4}\,J \rightarrow \text{Eqn. 7}$$

The total output electrical energy generated in one second can be expressed as the output electrical work done (W_e).

Thus,

$$W_e = 5.19 \times 10^{-4}\,Js^{-1} \rightarrow \text{Eqn. 8}$$

The Piezoelectric Nanogenerator device efficiency (PENG Efficiency) per second is, therefore, the output work efficiency (OWE) that can be calculated as the percentage ratio of W_e (From Eqn. 8) and W_d (From Eqn. 5)

$$OWE = \frac{W_e}{W_d}$$

$$\%OWE = \frac{W_e}{W_d} \times 100\,\%$$

$$\%OWE = \frac{5.19 \times 10^{-4}\,Js^{-1}}{1.79\ \times\ 10^{-3}Js^{-1}} \times 100\,\%$$

$$\%OWE = 28.99\,\%$$

$$\%OWE \simeq 29\,\%$$

Table S9. Comparison table of effective pressure, output V_{PP}, I_{PP} and output electrical energy of known organic composite energy harvesters.

Polymer composite compound devices	**Applied force, Frequency**	**Active area**	**Pressure**	**Output voltage**	**Current**	**Electrical energy**	**Efficiency**	**Ref.**
$[[Ni_6(H_2O)_{12}(TPTA)_8]\cdot(NO_3)_{12}\cdot 36H_2O]$/PDMS	21 N	2.0×2 cm^2	0.0525 MPa	25.25 V	18.76 µA	18.0 µJ	-	[10]
$[[Co_6(H_2O)_{12}(TPTA)_8]\cdot(NO_3)_{12}\cdot 50H_2O]$/PDMS	21 N	2.0×2 cm^2	0.0525 MPa	12.20 V	16.2 µA	-	-	[11]
$[Ph_2(^iPrNH)_2P]\cdot PF_6$/PDMS	15 N	1.8×1 cm^2	0.083 MPa	8.5 V	0.5 µA	4.25 µJ	-	[12]
DPDP.PF_6/PDMS	15N,10 Hz	1.3×3 cm^2	0.038 MPa	8.5 V	0.5 µA	4.25 µJ	-	[13]
TPAP.BF_4/TPU	22 N, 8 Hz	1.3×3 cm^2	0.056 MPa	7.37 V	0.61 µA	4.49 µJ	-	[14]
TIAP.BF_4/TPU	22 N, 8 Hz	1.3×3 cm^2	0.056 MPa	4.75 V	0.41 µA	1.95 µJ	-	[14]
DPDP.BF_4/TPU	22 N, 8Hz	1.3×3 cm^2	0.056 MPa	8.95 V	0.89 µA	7.96 µJ	-	[14]
$FAPbBr_3$/PDMS	-----	1×3 cm^2	0.5MPa	8.5 V	11.4 µA	96.9 µJ	-	[15]

[75 wt% (R-MBA) $PbBr_3$ + 25 wt% (R-MBA)PbI_3] /PCL	21 N, 8 Hz	2.5 × 2 cm^2	0.0336 MPa	40.8 V	0.06 µA	4.95 µJ	-	[16]
[(*S*)-NEA]$_4$[Bi_2Cl_{10}]/PCL	24 N, 8Hz	2.5 × 2 cm^2	0.0384 MPa	15.0 V	20.0 µA	0.50 µJ	-	[17]
[($PhCH_2NH)_6P_3N_3Me$]I, [PMe]I	21 N, 9 Hz	1.4 × 1.8 cm^2	0.0833 MPa	13.7 V	9.752 µA	133.6 µJ	-	[18]
DIPA·BNPP / PDMS	12 N, 8 Hz	2.5 × 2 cm^2	0.0192 MPa	9.5 V	7.7 µA	89.49 µJ	13.09 %	[9]
BzA·^{Cl}Ph-Cy-DMP /PCL	**30 N, 8 Hz**	2.5 × 2 **cm^2**	**0.048 MPa**	23.6 V	6.6 µA	-	~ 29 % at 9.8 N	**This Work**

TPTA = tris(3-aminopyridyl)thiophosphoramide DPDP·PF_6 = diphenyl diisopropylamino phosphonium hexaflurophosphate; TPU = thermoplastic polyurethane; DPDP·BF_4 = diphenyl diisopropylaminophosphonium tetrafluoroborate; TPAP·BF_4 = triphenyl isopropylaminophosphonium tetrafluoro borate; TIAP·BF_4 = tetraisopropylaminophosphonium tetrafluoro borate; Bn = benzyl; 4-BrBn = 4-bromobenzyl; (*S*)-NEA = (*S*)-1-(naphthalen-2-yl)ethan-1-ammonium; PCL = poly-caprolactone; R-MBA = (R)-alpha-methylbenylamine; PDMS = Polydimethylsiloxane.

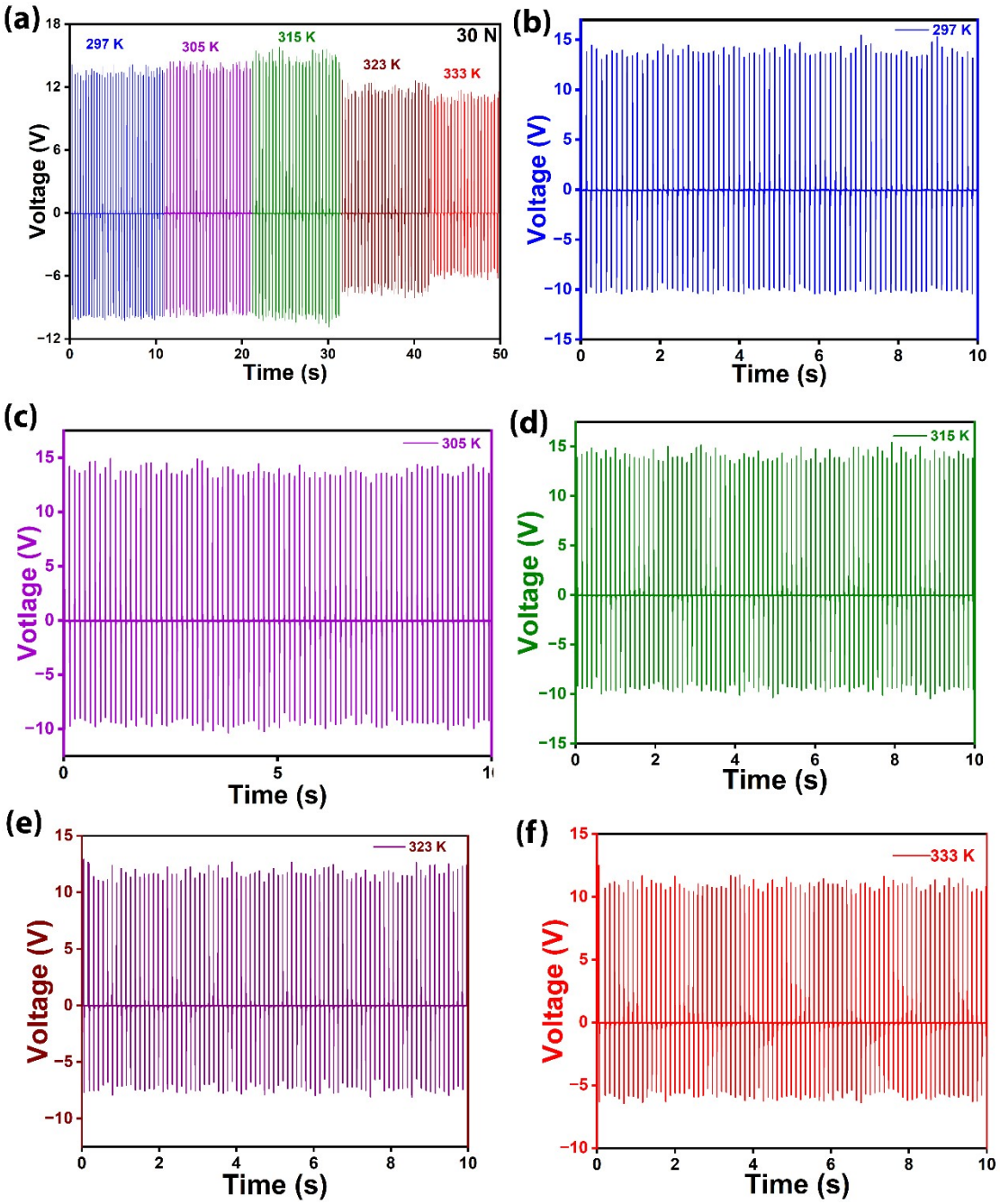

Figure S32. Temperature-dependent piezoelectric open circuit output voltage of 15 wt% **BzA·^{Cl}Ph-Cy-DMP**-PCL device showing the voltage versus time profiles at (a) 297 K,(b) 305 K, (c) 315 K, (d) 323 K, and (e) 333 K.

Table S10. Comparison table of effective change in energy harvesting properties of 15 wt% **BzA·^{Cl}Ph-Cy-DMP-** PCL device at 297 K and 333 K at a constant force of 30 N.

Serial No.	Properties	297 K	333 K	Change	Percentage Change (%)
1	Voltage	23.6 V	26.3 V	2.7 V	11.44
2	Current	6.6 µA	5.835 µA	0.765 µA	11.59
3	Power density	4.56 µW cm^{-2}	4.115 µW cm^{-2}	0.445 µW cm^{-2}	10.81
4	Current density	1.056 µA cm^{-2}	0.9336 µA cm^{-2}	0.1224 µA cm^{-2}	11.55
5	Response	20.1 ms	20.4 ms	--	--

Table S11: Interior and exterior angle strain around the O-P-O angle of **BzA·^{Cl}Ph-Cy-DMP.**

Serial No.	Temperature (K)	Angle Found (°)	Bond length (Å)	Angle Strain (kcal mol^{-1})
1	293	O-P-O$_{Interior}$ = 102.44156	1.5325	0.2979
		O-P-O $_{Exterior}$ = 116.15104	1.6200	0.2364
2	297	P-O-P $_{Interior}$ = 102.44156	1.5325	0.3798
		O-P-O $_{Exterior}$ = 116.14866	1.6200	0.3015
3	310	O-P-O $_{Interior}$ = 101.52454	1.5325	0.6701
		O-P-O $_{Exterior}$ = 116.68137	1.6200	0.7420
4	315	O-P-O $_{Interior}$ = 101.52454	1.5325	1.0227
		O-P-O $_{Exterior}$ = 116.68137	1.6200	0.7420
5	320	O-P-O $_{Interior}$ = 102.44286	1.5325	0.6258
		O-P-O $_{Exterior}$ = 116.15034	1.6200	0.4974
6	325	O-P-O $_{Interior}$ = 101.73436	1.5325	0.2302
		O-P-O $_{Exterior}$ = 116.60349	1.6200	0.1724
7	330	O-P-O $_{Interior}$ = 101.52426	1.5325	0.1985
		O-P-O $_{Exterior}$ = 116.68359	1.6200	0.1441

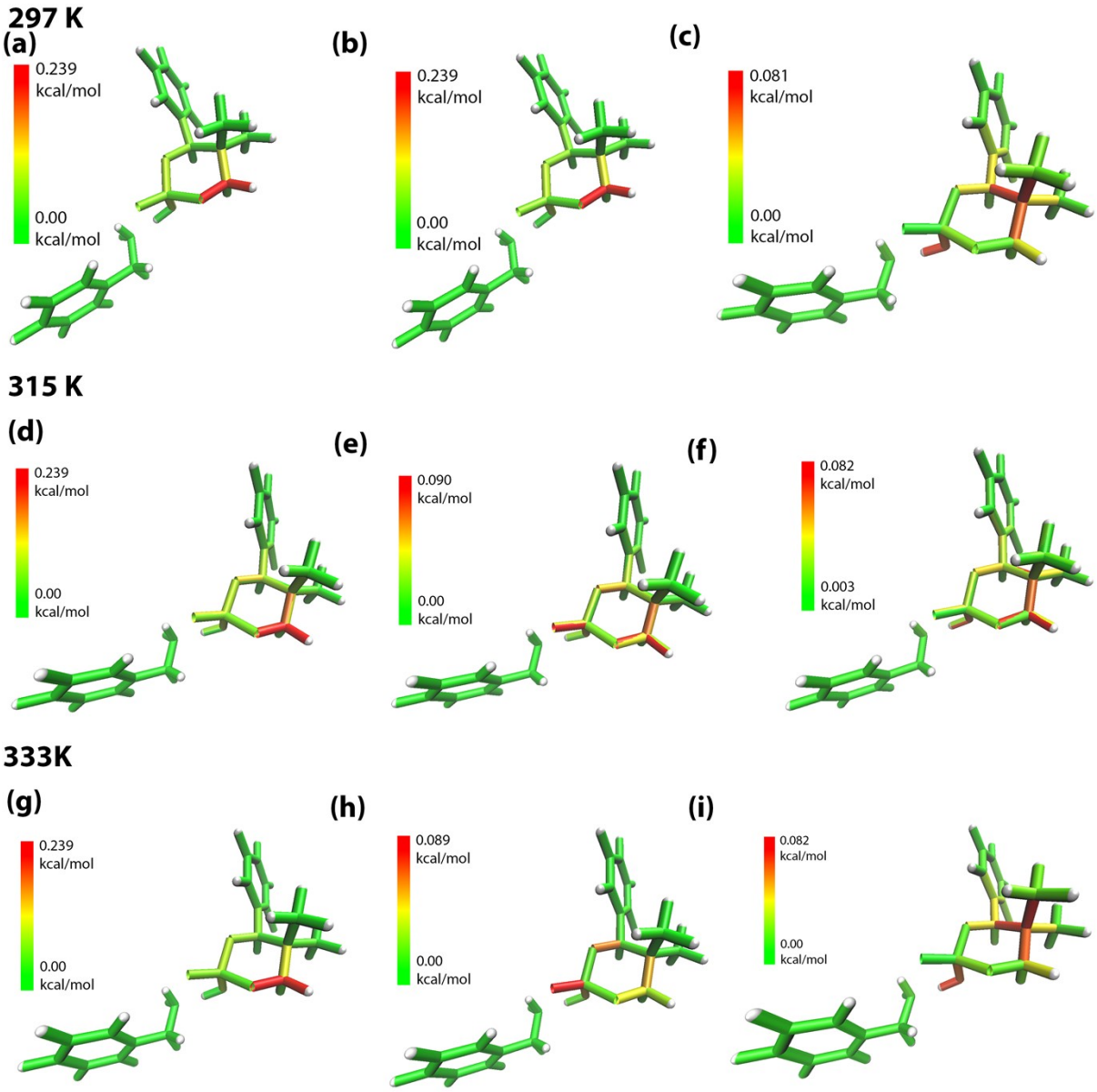

Figure S33. The visualization of the angle strain, bond strain and dihedral strain of **BzA-^{Cl}Ph-Cy-DMP**. (a), (b) and (c) are the angle strain, bond strain and dihedral strain at the 297 K. (d), (e) and (f) are the angle strain, bond strain and dihedral strain at 315K. (g), (h) and (i) are the angle strain, bond strain and dihedral strain at 333 K.

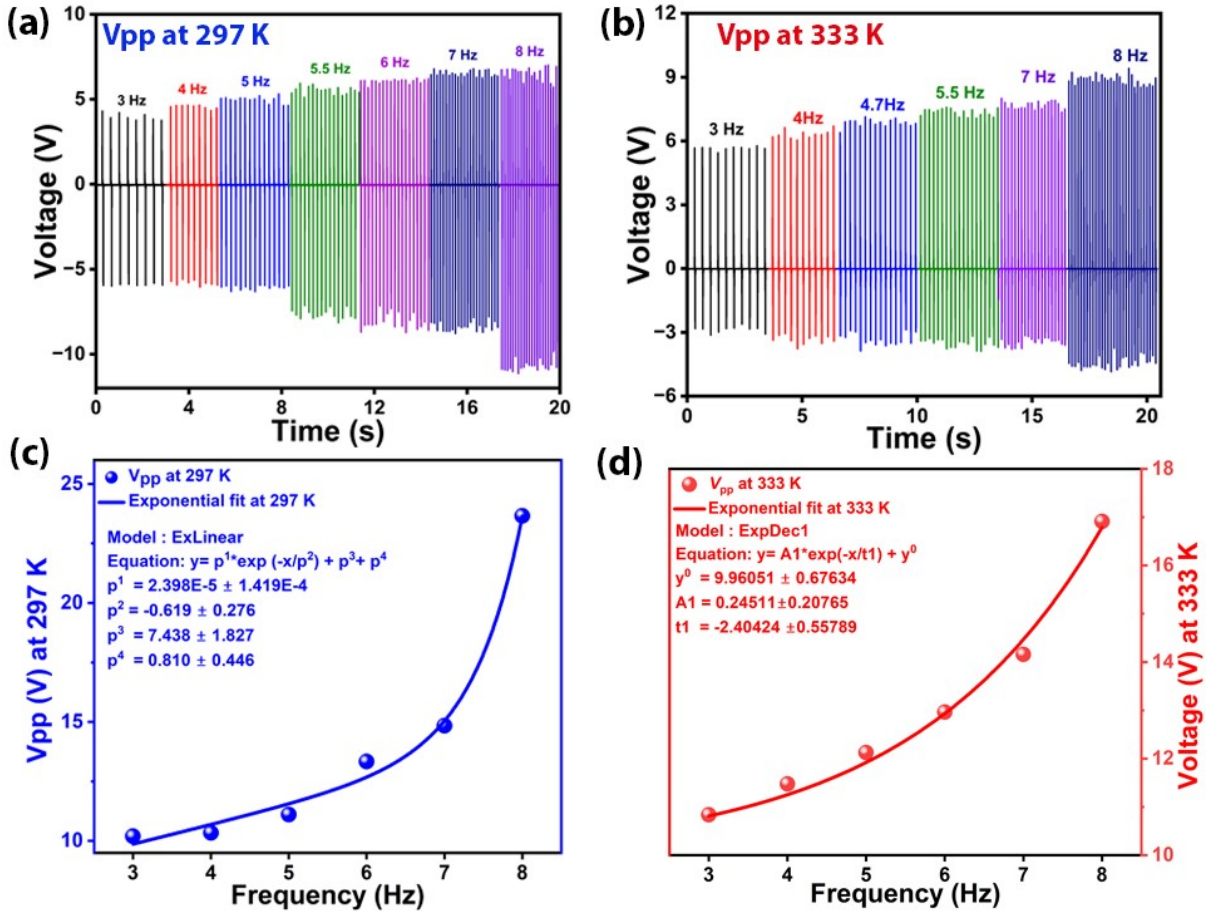

Figure S34. Frequency-dependent piezoelectric open circuit output voltage of 15 wt% **BzA·^{Cl}Ph-Cy-DMP**-PCl device at (a) 297 K and (b) 333 K. Fitted-graph of the open-circuit peak-to-peak voltage data of the 15 wt% **BzA·^{Cl}Ph-Cy-DMP**–PCL device under different frequencies at (c) 297 and (d) 333 K.

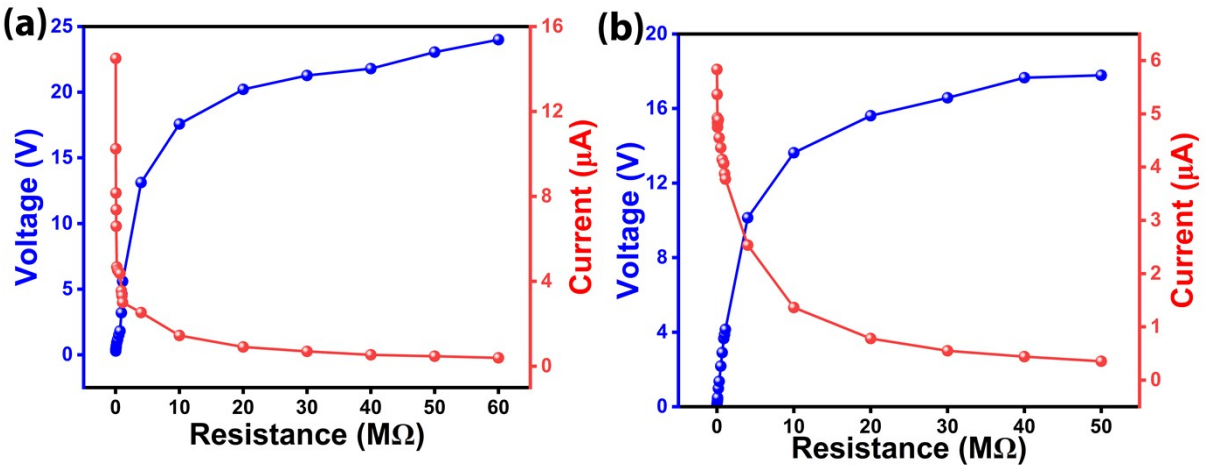

Figure S35. The current and voltage profiles of the 10 wt% 15 wt% **BzA·^{Cl}Ph-Cy-DMP**-PCl composite device under different external load resistances at 297 K and 333 K. The solid lines are the guide to the eye.

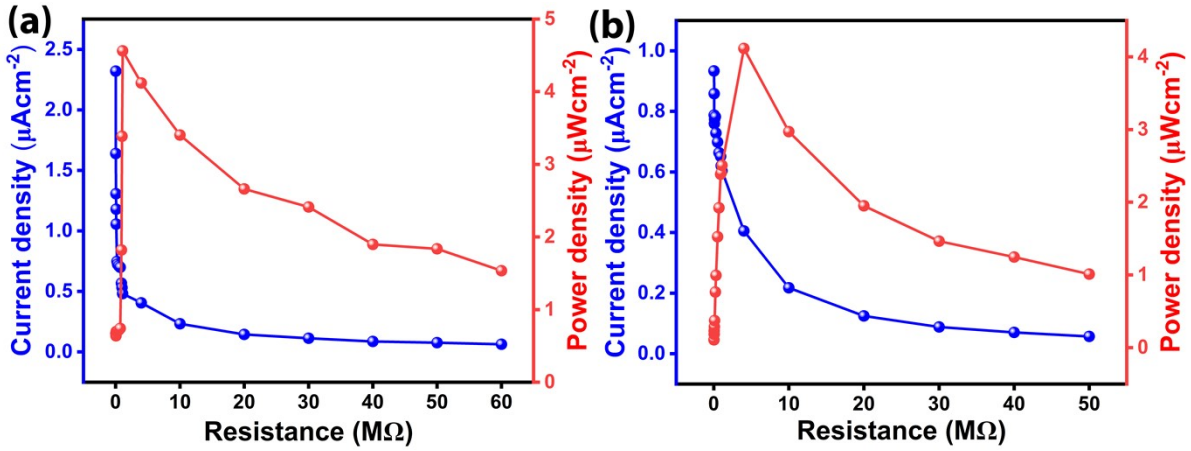

Figure S36. The current density and power density values of the 15 wt% **BzA·^{Cl}Ph-Cy-DMP**-PCL composite device under different external load resistances at (a) 297 K and (b) 333 K.

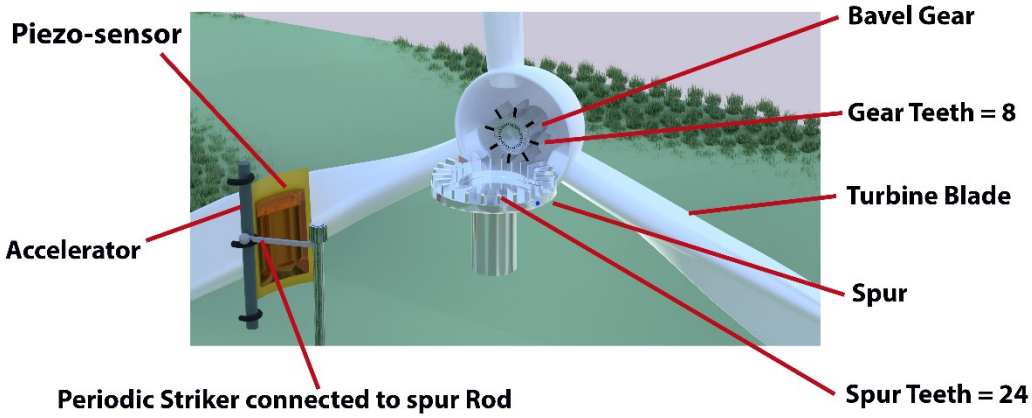

Figure S37. The schematic shows the working principle of the wind sensor and explains its operating mechanism.

Supporting Discussion 2: Wind flow (wind speed) calculation:

The wind flow sensing prototype was designed using a combination of spur and bevel gears to achieve both speed reduction and a 90° change in rotational direction.[19] The rotational speed of the wind turbine blades was reduced by a factor of three through this gearing mechanism. Consequently, a significant output signal was generated from the piezoelectric sensor. This configuration ensures that the piezoelectric sensor produces a single measurable signal for every three complete prototype wind turbine rotations.

Let Δt be the time interval of the turbine blade to complete one cycle, and Δt_1 be the time interval of the piezo-sensor to generate one complete signal.

$$\Delta t = \frac{1}{3} \times \Delta t_1 \text{ -----1}$$

Again, let us suppose v is the speed of the turbine blade, *r* is the radius of the wind turbine blade, and ω is the angular velocity of the turbine blade. Here, *r* is 11 cm.

$$blade\ speed\ (v) = r \times \omega$$

$$blade\ speed\ (v) = r \times \frac{2\pi}{\Delta t} \text{ ----2}$$

From equation (1)

$$v = 3 \times \frac{2\pi}{\Delta t_1} \times r$$

$$v = 207.24 \times \frac{1}{\Delta t_1} cm.s^{-1}$$

$$v = 2.0724 \times \frac{1}{\Delta t_1} m.s^{-1} \quad \text{------3}$$

The Tip-Speed Ratio (TSR), λ, is a dimensionless parameter that quantifies the relationship between the velocity at the tip of a wind turbine blade and the free-stream wind velocity.[20] It is mathematically expressed as:

$$TSR\ (\lambda) = \frac{v}{v_{wind}}$$

$$v_{wind} = \frac{v}{\lambda} \quad \text{------4}$$

Substituting equation 3 in equation 4, the wind flow velocity, v_{wind}, can be estimated from the equation 5 below.

$$v_{wind} = 2.0724 \times \frac{1}{\Delta t_1} \times \frac{1}{\lambda} m.s^{-1} \quad \text{------5}$$

From the calibrated commercial sensors, the TSR value was calculated to be 4. It is to be noted that both Δt and Δt_1 are variable parameters depending upon the speed of the blowing wind. It is noted that the TSR value is sensor-dependent and may vary with sensor configuration.

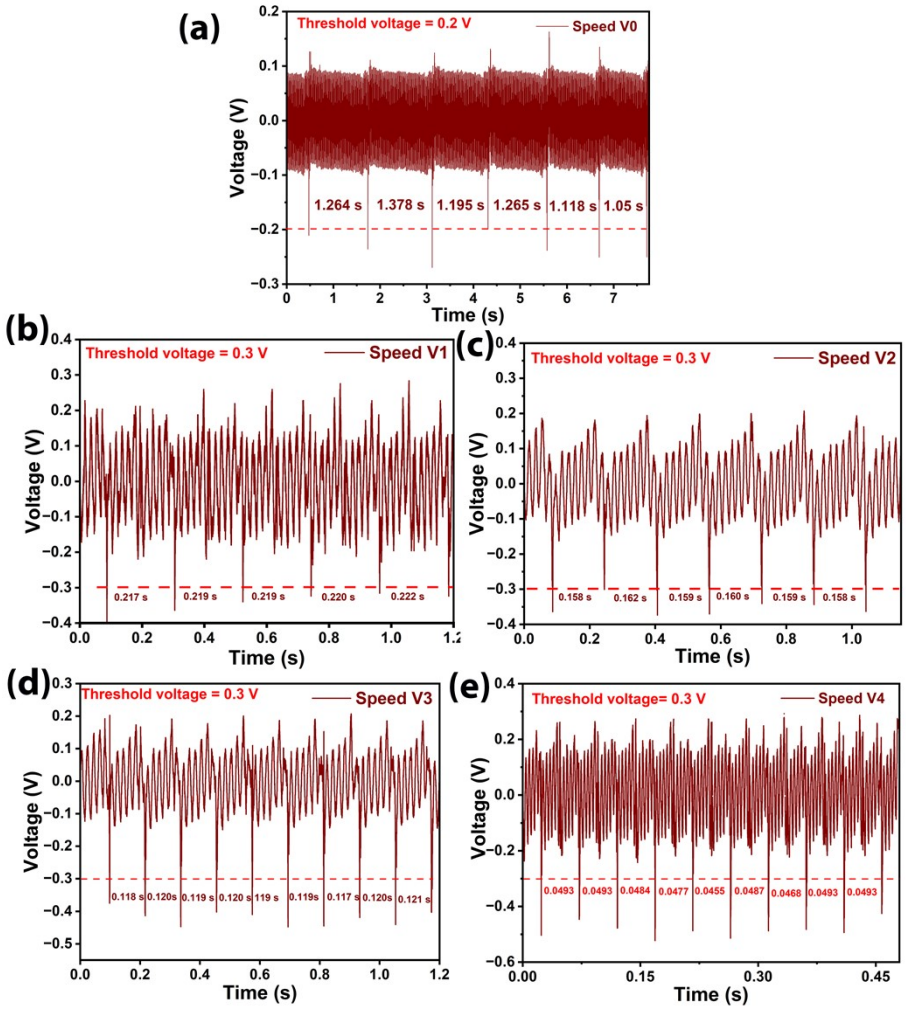

Figure S38. (a) The voltage-time response plot showing the minimum velocity V0 occurs at a threshold voltage of 0.2 V. (b)-(e) Voltage-time response plots for different velocity runs of V1, V2, V3, and V4 exhibiting pronounced signals at the threshold voltage of 0.3 V.

Table S12: Details of wind velocity calculation for various fan speeds.

Sr. no.	Time interval range (second)	Time interval (ΔT)	Speed $v_{wind} = 2.0724 \times \frac{1}{\Delta t_1} \times \frac{1}{\lambda} m.s^{-1}$	Standard deviation	Average speed of 3 consecutive lines ($m.s^{-1}$)
V0	1.7385-0.4748	1.264	0.41	0.025	0.41 ± 0.025
	3.1162-1.73854	1.378	0.38		
	4.31082-3.1162	1.195	0.43		
	5.57608-4.3108	1.265	0.41	0.041	0.45 ± 0.041
	6.6938-5.5761	1.118	0.46		
	7.7129-6.6938	1.049	0.49		
V1	0.3048 - 0.08745	0.217	2.40	0.017	2.38 ± 0.017
	0.5241 - 0.3048	0.219	2.37		
	0.7429 - 0.52413	0.219	2.37		
	0.9631 - 0.74286	0.220	2.36	0.014	
	1.1847 - 0.96304	0.222	2.34		
V2	0.08756 - 0.2451	0.158	3.28	0.042	3.25 ± 0.042
	0.40670 - 0.2451	0.162	3.20		

	0.56578 - 0.4067	0.159	3.26		
	0.7256 - 0.56578	0.160	3.24	0.02	3.26 ± 0.020
	0.88438 - 0.7256	0.159	3.26		
	1.04164 - 0.8843	0.158	3.28		
V3	0.2166 - 0.0983	0.118	4.39	0.035	4.35 ± 0.035
	0.3365 - 0.21658	0.120	4.32		
	0.4551 - 0.33654	0.119	4.35		
	0.57536 - 0.4551	0.120	4.32	0.017	4.34 ± 0.017
	0.6939 - 0.57536	0.119	4.35		
	0.81328-0.69392	0.119	4.35		
	0.93324-0.81328	0.120	4.32	0.023	4.31 ± 0.023
	1.05334-0.93324	0.120	4.32		
	1.1742-1.05334	0.121	4.28		
V4	0.07226-0.02293	0.0493	10.50	0.1151	10.57 ± 0.1151
	0.12158-0.0722	0.0493	10.50		
	0.16999-0.12159	0.0484	10.70		
	0.216587-0.1688	0.0477	10.84	0.3835	10.95 ± 0.3835
	0.262146-0.2165	0.0455	11.37		
	0.31389-0.26214	0.0487	10.62		
	0.36068-0.31389	0.0468	11.07	0.3699	10.83 ± 0.3699
	0.41147-0.36068	0.0498	10.40		
	0.45652-0.41147	0.0470	11.01		

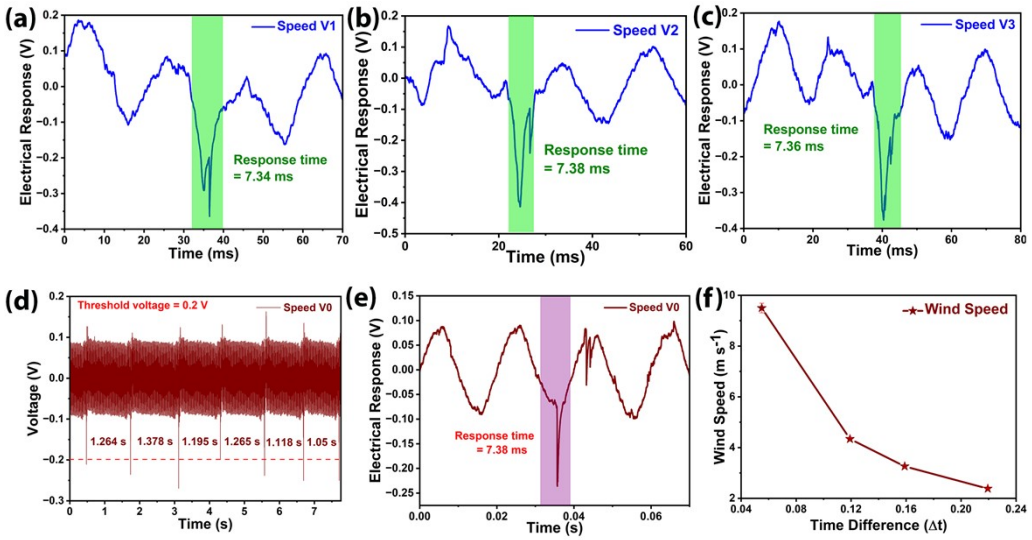

Figure S39. (a)–(c) Electrical response-time plots of V1, V2, and V3 showing the threshold signals at different velocities. (d) The voltage-time response plot indicates that the minimum velocity V0 occurs at a threshold voltage of 0.2 V. (e) The electrical response–time plot indicates a response time of 7.38 ms for signal detection. (f) The wind speed vs. time difference (Δt) between two consecutive signals shows an inverse trend.

Author contributions

R. B. and V.K. designed the project. V.K., D.Y.S, and A.K prepared the samples and did the measurements. V.K. and R. B. performed the piezoelectric energy harvesting measurements and analysis. J.K.Z. performed non-linear optical measurements. V.K., and R.B. wrote the original manuscript. S.K.M, and J.K.Z. reviewed and edited the manuscript. R. B. directed the project. All the authors discussed the results and contributed sincerely to the preparation of the manuscript.

References

1. G. M. Sheldrick, *Acta Crystallogr., Sect. C*, 2015, **71**, 3-8.
2. W. T. Pennington, *Acta Crystallogr., Sect. A*, 1999, **32**, 1028-1029.
3. L. J. Farrugia,*J. Appl. Crystallogr.*, 1999, **32**, 837-838.
4. P. R. Spackman, M. J. Turner, J. J. McKinnon, S. K. Wolff, D. J. Grimwood, D. Jayatilaka and M. A. Spackman, *J. Appl. Crystallogr.*, 2021, **54**, 1006-1011.
5. S. Kurtz and T. Perry, *J. Appl. Phys.*, 1968, **39**, 3798-3813.
6. M. Frisch, *Inc, Wallingford CT*, 2009, **201**.
7. C. E. Colwell, T. W. Price, T. Stauch and R. Jasti, *Chem. Sci.*, 2020, **11**, 3923-3930.
8. W. Humphrey, A. Dalke and K. Schulten, *J. Mol. Graph.*, 1996, **14**, 33-38.
9. V. Kushwaha, N. Prajesh, A. Gopal, S. Sahoo, S. Deswal, A. Kirana, K. Shanmuganathan, J. K. Zaręba and R. Boomishankar, *J. Mater. Chem. A* , 2025, **13**, 22574-22582.
10. N. Prajesh, D. R. Naphade, A. Yadav, V. Kushwaha, B. Praveenkumar, J. K. Zaręba, T. D. Anthopoulos and R. Boomishankar, *Chem. Commun.*, 2023, **59**, 2919-2922.
11. N. Prajesh, V. Kushwaha, D. R. Naphade, B. Praveenkumar, J. K. Zareba, T. D. Anthopoulos and R. Boomishankar, *ACS Appl. Energy Mater.*, 2025, **8**, 4648-4655.
12. T. Vijayakanth, F. Ram, B. Praveenkumar, K. Shanmuganathan and R. Boomishankar, *Angew. Chem. Int. Ed.*, 2020, **59**, 10368-10373.
13. A. Graja, *physica status solidi (b)*, 1968, **27**, K93-K97.
14. T. Vijayakanth, A. K. Srivastava, F. Ram, P. Kulkarni, K. Shanmuganathan, B. Praveenkumar and R. Boomishankar, *Angew. Chem. Int. Ed.*, 2018, **130**, 9192-9196.
15. T. Vijayakanth, F. Ram, B. Praveenkumar, K. Shanmuganathan and R. Boomishankar, *Chem. Mater.*, 2019, **31**, 5964-5972.
16. U. Makhija, V. Kushwaha, N. Prajesh, A. Nag and R. Boomishankar, *J. Mater. Chem. C*, 2025, **13**, 23037-23043.
17. S. K. Mahato, V. Kushwaha, J. K. Zareba and R. Boomishankar, *Inorg. Chem.*, 2025, **64**, 21194-21203.
18. A. Sultana, S. K. Ghosh, M. M. Alam, P. Sadhukhan, K. Roy, M. Xie, C. R. Bowen, S. Sarkar, S. Das and T. R. Middya, *ACS Appl. Mater. Interfaces*, 2019, **11**, 27279-27287.
19. S. Priya and D. J. Inman, *Energy harvesting technologies*, Springer, 2009.
20. J. F. Manwell, J. G. McGowan and A. L. Rogers, *Wind energy explained: theory, design and application*, John Wiley & Sons, 2010.